MICROCOPY RESOLUTION TEST CHART

NATIONAL BUREAU OF STANDARDS 1963 A

Proof-of-Principle High Speed Electronic Imaging System-Phase II

David M Holt

AD-A193 798

LOS ALAMOS NATIONAL LABORATORY
LOS ALAMOS, NEW MEXICO 87545

DTIC

S ELECTE D
APR 2 7 1988

D

MARCH 1988

FINAL REPORT FOR PERIOD OCTOBER 1984-OCTOBER 1987

APPROVED FOR PUBLIC RELEASE; DISTRIBUTION UNLIMITED

AIR FORCE ARMAMENT LABORATORY

Air Force Systems Command ∎ United States Air Force ∎ Eglin Air Force Base, Florida

88 4 26 129

NOTICE

When Government drawings, specifications, or other data are used for any purpose other than in connection with a definitely Government-related procurement, the United States Government incurs no responsibility nor any obligation whatsoever. The fact that the Government may have formulated or in any way supplied the said drawings, specifications, or other data, is not to be regarded by implication or otherwise in any manner construed, as licensing the holder, or any other person or corporation; or as conveying any rights or permission to manufacture, use, or sell any patented invention that may in any way be related thereto.

The Public Affairs Office has reviewed this report, and it is releasable to the National Technical Information Service (NTIS), where it will be available to the general public, including foreign nationals.

This technical report has been reviewed and is approved for publication.

FOR THE COMMANDER

LAWRENCE W. KETTER, Col, USAF
Chief, Aeromechanics Division

Please do not request copies of this report from the Air Force Armament Laboratory. Copies may be obtained from DTIC. Address your request for additional copies to:

> Defense Technical Information Center
> Cameron Station
> Alexandria, VA 22304-6145

If your address has changed, if you wish to be removed from our mailing list, or if your organization no longer employs the addressee, please notify AFATL/FXA , Eglin AFB FL 32542-5434, to help us maintain a current mailing list.

Copies of this report should not be returned unless return is required by security considerations, contractual obligations, or notice on a specific document.

REPORT DOCUMENTATION PAGE

Form Approved
OMB No. 0704-0188

1a. REPORT SECURITY CLASSIFICATION	1b. RESTRICTIVE MARKINGS
Unclassified	

2a. SECURITY CLASSIFICATION AUTHORITY	3. DISTRIBUTION / AVAILABILITY OF REPORT
	Approved for public release; distribution is unlimited
2b. DECLASSIFICATION / DOWNGRADING SCHEDULE	

4. PERFORMING ORGANIZATION REPORT NUMBER(S)	5. MONITORING ORGANIZATION REPORT NUMBER(S)
	AFATL-TR-88-14

6a. NAME OF PERFORMING ORGANIZATION	6b. OFFICE SYMBOL (If applicable)	7a. NAME OF MONITORING ORGANIZATION
Los Alamos National Laboratory		Aerodynamics Branch Aeromechanics Division

6c. ADDRESS (City, State, and ZIP Code)	7b. ADDRESS (City, State, and ZIP Code)
Group MEE-3, MS J580 Los Alamos, NM 87545	Air Force Armament Laboratory Eglin AFB, FL 32542-5434

8a. NAME OF FUNDING / SPONSORING ORGANIZATION	8b. OFFICE SYMBOL (If applicable)	9. PROCUREMENT INSTRUMENT IDENTIFICATION NUMBER
Aeromechanics Division	AFATL/FXA	MIPR FY7621-87-90042

8c. ADDRESS (City, State, and ZIP Code)	10. SOURCE OF FUNDING NUMBERS			
Air Force Armament Laboratory Eglin AFB, FL 32542-5434	PROGRAM ELEMENT NO.	PROJECT NO.	TASK NO	WORK UNIT ACCESSION NO.
	62602F	2567	03	01

11. TITLE (Include Security Classification)

Proof-of-Principle High Speed Electronic Imaging System - Phase II

12. PERSONAL AUTHOR(S)

David M. Holt

13a. TYPE OF REPORT	13b. TIME COVERED	14. DATE OF REPORT (Year, Month, Day)	15. PAGE COUNT
Final	FROM Oct 84 TO Oct 87	March 1988	73

16. SUPPLEMENTARY NOTATION

Availability of this report is specified on verso of front cover.

17.	COSATI CODES		18. SUBJECT TERMS (Continue on reverse if necessary and identify by block number)
FIELD	GROUP	SUB-GROUP	Shadowgraph System, Electronic Imaging, High Speed Data Processing, Free Flight Testing, Ballistic Spark Range

19. ABSTRACT (Continue on reverse if necessary and identify by block number)

The feasibility of using electronic imaging technology for aeroballistics research has been proven with the installation and testing of the High Speed Electronic Imaging System at the Eglin Aeroballistics Research Facility. Test results obtained using the system have produced high resolution data with the accuracy and precision required in the Aeroballistics Research Facility.

20. DISTRIBUTION / AVAILABILITY OF ABSTRACT	21. ABSTRACT SECURITY CLASSIFICATION
☐ UNCLASSIFIED/UNLIMITED ☒ SAME AS RPT. ☐ DTIC USERS	Unclassified

22a. NAME OF RESPONSIBLE INDIVIDUAL	22b. TELEPHONE (Include Area Code)	22c. OFFICE SYMBOL
R. J. Kelley	(904) 882-4086	AFATL/FXA

DD Form 1473, JUN 86   Previous editions are obsolete.

PREFACE

This program, known internally as the electronic shadowgraph project, was conducted by the Los Alamos National Laboratory, Los Alamos, New Mexico 87545, under a Memorandum of Agreement (MIPR FY7621-87-90042) with the Air Force Armament Laboratory, Eglin Air Force Base, FL 32542-5434. Mr. R.J. Kelley (AFATL/FXA) managed the program for the Armament Laboratory.

The program was conducted during the period from October 1984 to October 1987.

As always, projects like this are not done by one person. A lot of other people, both at Los Alamos and at Eglin have contributed in significant ways, and should be recognized for their participation and contributions to the work done.

Special acknowledgment should be given to Robin Morel, who coded the algorithms and implemented the operating menu within the "Imagelab" software.

Those whose contributions were very helpful in the project are acknowledged:

Los Alamos	Eglin	Megavision
Robin Morel	R.J. Kelley	Don Roberts
Tom Kuckertz	Jerry Winchenbach	George Streckmann
Martha Martinez	John Krieger	
Joe Parker	John Morris	
	Ann Coverston	
	Karen Hollis	
	Gregg Abate	

A-1

TABLE OF CONTENTS

LIST OF FIGURES

LIST OF TABLES

SECTION I

INTRODUCTION

A detailed analysis of the requirements for an electronic shadowgraph system in the Aeroballistics Research Facility, located at the Eglin Air Force Base, Ft. Walton Beach, Florida, was performed in 1985 and presented at the International Congress on Instrumentation in Aerospace Simulation Facilities (ICIASF) meeting (Reference 1) at Stanford University in August, 1985. Briefly, the facility is 680 feet long and 12 feet wide for the first one third of the range, and 16 feet wide for the last two thirds. Projectiles and models of various shapes are fired down the range and photographed at 50 stations along the range to determine their stability, aerodynamic properties and other flight characteristics. Each imaging station along the range, shown in Figure 1, captures two orthogonal shadowgraph images of the projectile as it passes.
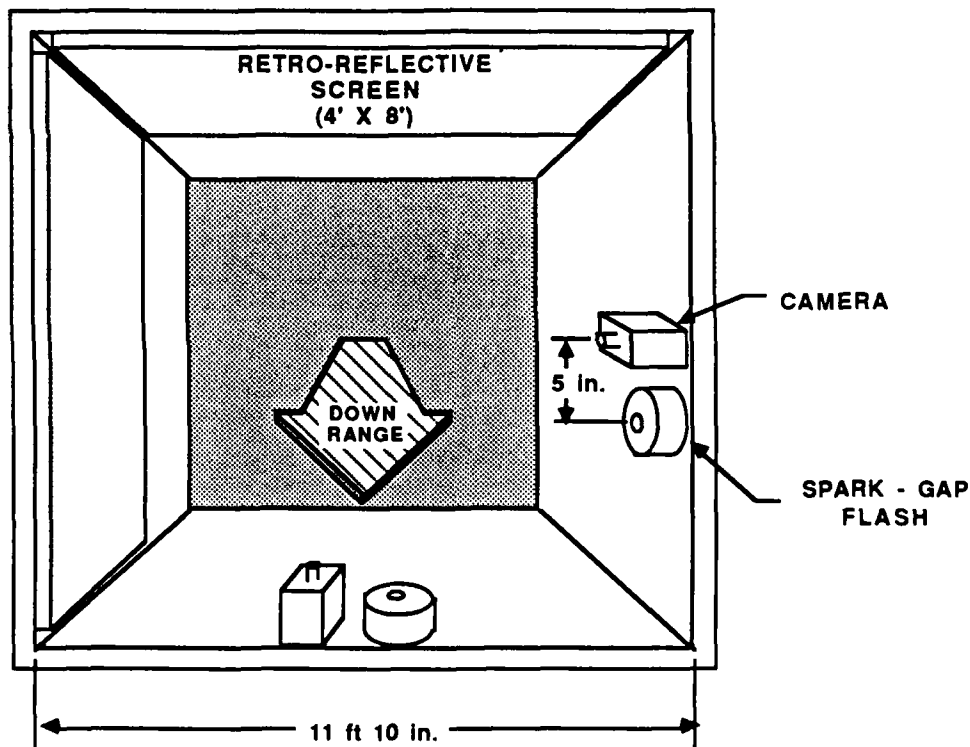
Figure 1. Typical Shadowgraph Station

1

The objective of the analysis was to provide system requirements and a conceptual design of a state-of-the-art high-speed electronic imaging system to improve the data acquisition and analysis of projectiles in flight. The projectiles vary in shapes and may travel at speeds up to MACH 6. The required resolution was determined by measuring the transfer function and optical illumination parameters of the existing system.

From the transfer function, the limiting resolution was determined to be 0.72 cycles per millimeter at the reflective screen. Illumination parameters were determined to ascertain the usefulness of the available spark-gap light source for large area arrays. Intensity and spectral characteristics of the source were measured.

Based on the analysis, a prototype was developed to verify the analysis and to determine if projectile points of interest can be located with the desired accuracy. The prototype system described in Sections II and III acquires images at only one station. Static projectile images were successfully acquired using modified Westinghouse vidicon cameras and a VICOM image processing system. However, the vidicon cameras were not sensitive enough to image with the Eglin spark-gap.

A re-evaluation of the project, based on the failure of the vidicon cameras and associated high cost of comparable charge-coupled device (CCD) cameras, resulted in evaluating various algorithms for making projectile measurements which would reduce the resolution requirements. Two of those algorithms are described in Section V.

Section VI describes the method, and derives the equations, for locating a projectile in 3-space from the centroid and second moment of inertia data taken from two orthogonal shadowgraphs with an electronic camera.

As a result of the promise of the resolution reducing algorithms, a proof-of-principle imaging system was assembled and installed at the Eglin Aeroballistics Research Facility. Images on various shots were successfully acquired using the Eglin spark-gap, and a few measurements were made to compare accuracy with the film cameras. Section VII describes that system and the results of comparisons with film measurements.

SECTION II

EARLY PROTOTYPE

The early prototype system consisted of two Westinghouse vidicon cameras, an image processing system, a spark-gap light source, an infrared linear array motion detector, and a retro-reflective screen on which a shadowgraph is formed.

1. CAMERAS

A large area array detector of 2000 elements high and 1000 elements wide will almost satisfy the resolution requirements for the Eglin range (Reference 1). The cameras initially chosen were Westinghouse model ETV-2000 slow scan vidicons, modified to output a 2048_v x 1024_h image. When they were selected, they were the only cameras known that would approximate the resolution requirements. The cameras are operated in an "integrate mode" (open shutter) in total darkness. They are erased just prior to firing the projectile, and the image is acquired when the infrared motion detector senses the projectile and triggers the spark-gap light source. As soon as the light source is triggered, the image on the vidicon is scanned in about 0.5 seconds and sent as single frame video to be digitized by the image processor.

2. IMAGE PROCESSOR

The image processor is a VICOM Systems model 1800, which is a microprocessor based system. The system has image memory space for two 2048_v x 1024_h x 16 bit images, for a total of 4 mb. The image processor has a 50 mb hard disk, printer, console, and a color monitor capable of displaying a 512_v x 512_h pixel color image. Image processing software is also included, which allows a variety of processing operations such as filtering, image arithmetic, morphological, and graphical, to be performed on images either interactively or as a subroutine called from other software.

3. SPARK-GAP LIGHT SOURCE

An open air spark-gap, Hi-Voltage model SS55P, with a capacitor discharge circuit charged to 4800 vdc is employed as a strobed light source. The spark is discharged across a 2.2 mm air path, which is small enough to be considered as a point light source. The spark-gap is positioned adjacent to each camera and casts a well-defined shadow on the reflective screen. The spectral characteristics were reported in the 1985 ICIASF paper (Reference 1). The output of the spark-gap has a duration of about 300 nanoseconds. This duration is short enough to "stop" a projectile travelling at Mach 6.

4. INFRARED ARRAY TRIGGER

A narrow infrared beam about 8 feet high is projected onto the retro-reflective screen in order to detect the arrival of the projectile at a station. When the projectile enters the beam, a trigger is generated to flash the spark-gap light source.

5. RETRO-REFLECTIVE SCREEN

A 3M No. 7610 screen, made up to tiny glass beads about 0.002" in diameter, is used as the surface on which a shadow of the projectile is cast. The shadowgraph formed allows the camera to be focused on a known object (screen) since the projectile can be anywhere in the 12 foot width of the range. Since the screen is retro-reflective, light from adjacent stations is not reflected to the wrong camera. Also, the screen has a light gain over that of a Lambertian surface. The gain is dependent on the viewing angle to the source. A gain of about 40 is obtained in the Eglin range with the spark separated by 5" from the camera viewing axis, but a gain of about 1600 is possible if the light source is viewed on axis with the camera. The light gain of the screen vs. viewing angle is shown in Figure 2.
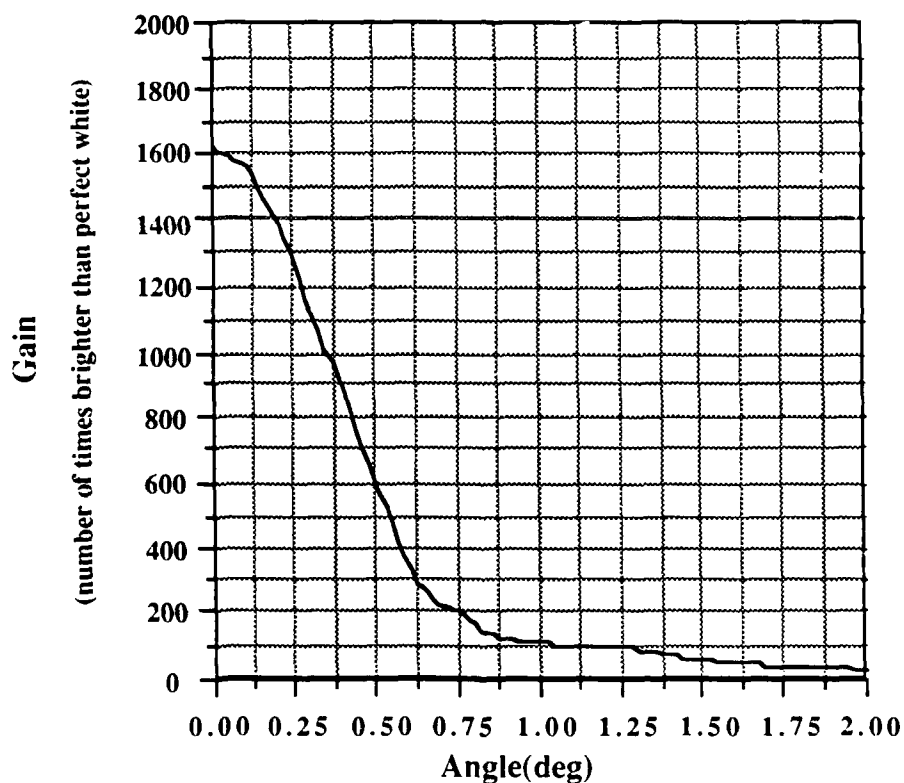
Figure 2. 3M Screen Data

4

SECTION III

EARLY PROTOTYPE RESULTS

Many tests of the vidicon cameras and system were done on a static projectile hanging in a simulated station at Los Alamos, complete with screen, spark-gap, and infrared trigger. Also, other measurements were done on the cameras and spark-gap, and some image processing has been done for image enhancement of the images produced. Some of the results are reported here.

1. SYSTEM

The system was assembled as described in Section II. Many non-shadowgraph images were obtained using overhead room lighting and timed exposures. The cameras were adjusted for optimal image quality and sensitivity. Software was written to monitor two signals (start and stop) for image acquisition, and then to store the images in memory. Displayed on the 19" monitor were 512 x 512 portions of the 2048 x 1024 images.

2. LIGHTING

An attempt was then made to obtain shadowgraph images using the spark-gap as the light source, with discouraging results. No image! The sensitivity of the camera was measured, using a TV Optoliner operated at 2856 °K color temperature and neutral density filters. The measured sensitivity was close to the manufacturer's data. The output of the spark-gap was then measured (Reference 2) both spectrally and for total energy using a spectrometer and a wavelength independent joulemeter for pulsed sources. The output of the spark-gap was determined to be about 10 microjoules, which is about a factor of 500 less than that determined in the initial study of the range parameters. Figure 3 shows the new spectral measurement on the spark-gap, which is quite different than the initial measurement in that it does not extend nearly as far into the red. This probably accounts for the disparity in the output intensity.
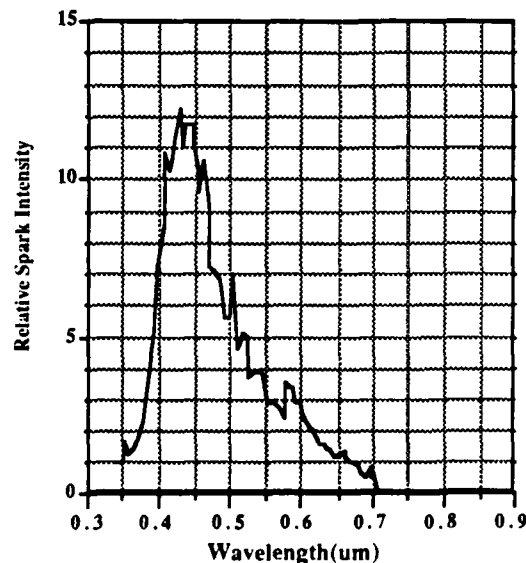
Figure 3.   Spark-Gap Intensity vs. Wavelength

3. RESOLUTION

The system resolution was measured (Reference 3) using a TV Optoliner to produce an image of a standard TV resolution chart. This image was focused directly on the vidicon tube of the camera, to get resolution independent of the lens, since the lens contribution could be readily determined. The results of the measurements show a resolution of about 0.82 Line Pair/mm at the screen, which meets the requirements of the system determined in the initial study. Additionally, another test showed that we could detect and locate a 1 mm diameter pin (used for determining spin or rotation of the projectile) which was another requirement of the range. This indicates that the initial range resolution measurement and determination of the electronic image resolution requirements was correct.

4. COST

One of the objectives of the prototype system was to demonstrate the feasibility of instrumenting the entire range at Eglin with a high speed electronic imaging system. The major benefits of doing this would be to dramatically reduce the time from a test to when results would be available. This could literally change the data reduction time from weeks to hours! For a test which requires several set-up shots, with time gains on each shot, the benefits are compounded.

The cost of each camera was about $25,000 in small quantities. It was estimated that for the 100 cameras required to instrument the range, the cost could be reduced to about $10,000 per camera (no guarantee), but that an image buffer would be required for each camera, since the image processor could not read the images from 100 cameras fast enough to prevent intolerable dark current contributions to image noise. So a cost of about $15,000 per camera and image buffer was estimated, which results in a system cost that exceeds the Eglin budget for the Aeroballistics Facility conversion.

5. SUMMARY

Results of the first measurements on the prototype system were very disappointing. Both from a performance standpoint and from a potential cost standpoint. The idea of replacing, or at least augmenting, the film camera system is a good one. Higher productivity, shortening the data reduction time and improving repeatability of measurements all seem to be possible with an electronic shadowgraph system. Unfortunately, cameras with cost to fit the Eglin budget and to do the job do not seem imminent within the next few years.

Therefore, at this stage, it seemed that unless another cost effective method could be found to make Aeroballistics measurements to the same accuracy as the current film method, the project must be abandoned. Also, the prototype system cannot be used to even demonstrate the feasibility of the electronic shadowgraph method, since the cameras are not sensitive enough to be used with the existing spark-gap light source.

SECTION IV

PROJECT RE-EVALUATION

At this point in the prototype development project, it was decided that we must re-evaluate some of the initial decisions and project direction. Some of the most pressing topics to be considered were:

1. COST

The Eglin project management has already projected that a cost of no more than $10,000 per camera/image buffer is the budget limit. CCD cameras now having the required resolution, available from only one source, and image memory will cost at least twice that much. Since costs of CCD cameras with array formats larger than 1024 x 1024 are not anticipated to be driven lower by the commercial market, we do not think that the cost of 2048 x 1024 cameras will be reduced appreciably in the near future.

2. CCD vs. VIDICON CAMERAS

There are several reasons to prefer CCD cameras over vidicons for our application. First, the geometric distortion in CCD cameras is practically zero, while there is about 1 to 3 percent in vidicons, which would have to be corrected. Also, CCDs do not have the blooming problem that vidicons have, and are usually smaller and more rugged than vidicons.

Additionally, a test was conducted on a standard CCD camera showing that it did have enough sensitivity to be used with our spark-gap light source, whereas the vidicon did not. So, CCDs are to be chosen as the preferred technology for the Eglin cameras, meaning further vidicon camera experiments would not be productive, since noise and imaging features would be different.

3. IMAGING REQUIREMENTS

The initial study determined the resolution capability of the existing film system and then proposed to replace it with a comparable electronic imaging system. However, those stringent resolution requirements result in requiring cameras that are too expensive. Instead of just duplicating the film system capability, we looked at what actually is needed at the Eglin range. It was determined that the basics of what was needed, was to very accurately determine the absolute position of the projectile and its orientation (pitch, yaw, and roll) at each station. The accuracy requirements of those measurements was next determined.

The pitch and yaw of a projectile is now determined geometrically at Eglin. Since most models are symmetrical about one or more axis, a point at the front tip and at the tail on the same axis are determined. The angle of the line connecting these points is the angle of the projectile. Since the images are actually projections of an object on a shadowgraph, three-dimensional geometry is required to determine the actual angle of the projectile from two orthogonal shadowgraph views of the same projectile. The accuracy requirements of determining the angle of the projection can be determined from the range requirements.

Figure 4 shows a model projection with front (F) and rear (R) points selected, and a line drawn between them. A grid is superimposed to represent a 2048$_v$ x 1024$_h$ array used to acquire the image.
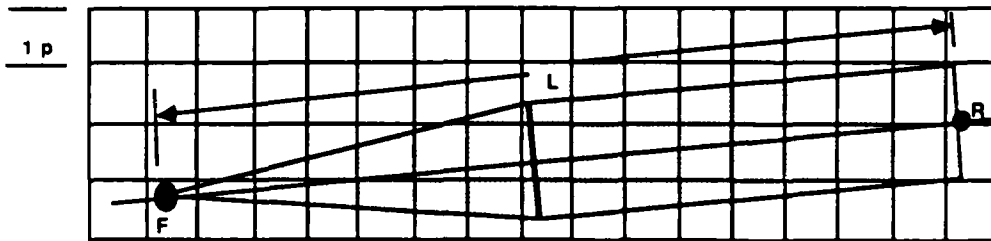
Figure 4. Model Projection

The error in determining the actual location of a point on the projectile is approximately +/- 0.5 pixel. The maximum error of the angle of the line connecting the two points F and R is described by the equation:

$$Error_{max} = SIN^{-1} \frac{+/- 1p}{L} \quad (degrees)$$

(1)

where p is the spatial dimension of a pixel and L is the length of the projectile. For the Eglin range, the shadowgraph screen measures 2438.4 mm (96") high x 1219.2 mm (48")wide. The 1219.2 mm dimension at the screen maps onto the 1024 pixel dimension of the array, thus the horizontal spatial dimension of each pixel is:

$$p = \frac{1219.2 \text{ mm}}{1024} = 1.19 \frac{mm}{pixel}$$

(2)

The vertical spatial pixel dimension is the same as the horizontal.

The shortest projectile tested and measured at the Eglin range is about 80 mm long x 20 mm diameter. Using Equation 2 for the pixel spatial dimension and L = 80 mm in Equation 1, we get an angular error of +/- 0.853 degrees for the shortest projectile. Keep in mind that this is the error when the front and rear points are located with no error. A one pixel error (operator error) in locating the front and rear points could result in three times the error determined above. However, for the comparison with the electronic imaging system we will assume that there is no location error. The angular error of +/- 0.853 degrees for the shortest projectile is the error that the electronic imaging system must achieve to match the 2048$_v$ x 1024$_h$ array.

4. IMAGE PROCESSING REQUIREMENTS

In the electronic imaging system, noise affects the accuracy of the processing algorithms, so any noise minimization will be helpful. This requires filtering or other noise reducing techniques to be used, and places a great emphasis on careful selection of image processing techniques that must be employed to provide a clean image while not affecting measurement accuracy. Also, if the background noise can be eliminated (by image processing), then the entire image can be processed instead of having to find the projectile. This can greatly simplify any image processing which automatically finds the projectile and determines its location and orientation.

SECTION V

REDUCING RESOLUTION REQUIREMENTS

Two primary methods have been investigated to reduce the resolution requirements to allow using a lower resolution (and thus lower cost) camera at the range. These methods are: finding centroids (first moment of inertia) and second moments of inertia of areas. An example of using the centroid to more accurately locate an object is demonstrated with the reference beads.

One of the tasks of any imaging system at the Eglin range is to accurately locate reference beads strung on Kevlar lines at each station, as shown in Figure 5, in order to locate the projectile shadowgraph with respect to the beads, and thus the absolute location in the range.
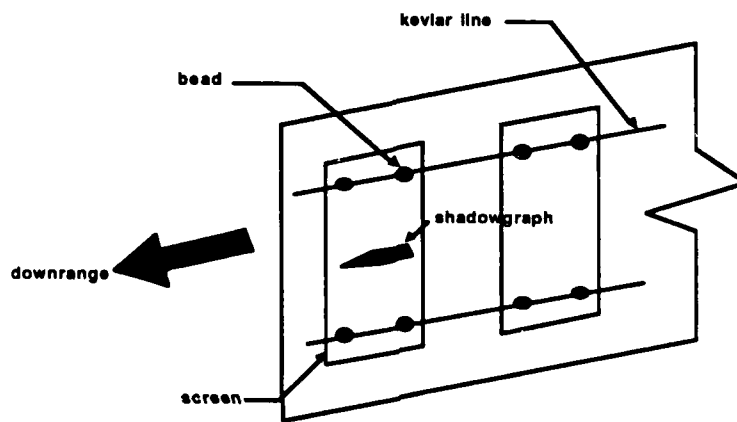
Figure 5. Shadowgraph Station Reference Beads

The absolute location of all beads in the range are accurately known, and thus provide a reference for determining the absolute location of the projectile shadowgraph, since both the reference bead, Figure 6, and projectile shadowgraph are contained in the same image.
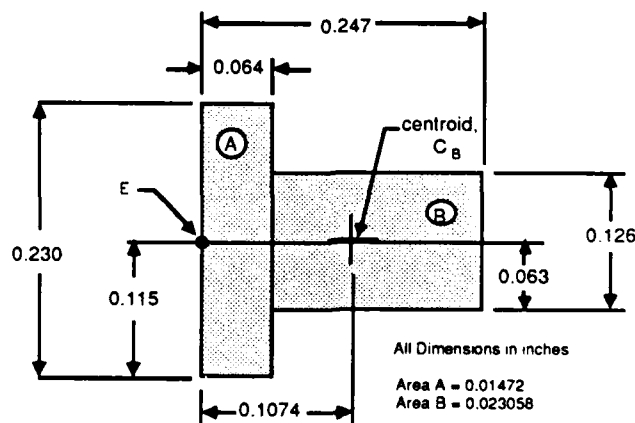
Figure 6. Eglin Bead

9

The projected area of the bead on the screen is about the same size as the bead, or 24.373 mm^2. Since the bead is located about 1/4" from the screen, there is very little magnification of the shadow over the actual bead size. The bead projected area covers about 17 square pixels in a 2048 x 1024 array ($24.373 \div p^2 = 17.2$). Locating an edge of the bead by locating a point (without further image processing) would still have a +/- 0.5 pixel error, or about +/- 0.595 mm (0.0234") error.

However, locating the centroid of the bead projection on the shadowgraph is much more accurate than the geometric method described above. Each pixel of the bead image is digitized to 12-bit accuracy (i.e., 1 part in 4096) in the VICOM system. The numerical value of the pixel (values between 0 and 1) represents the pixel area covered by the image, with 1 = fully covered. If the signal-to-noise ratio of the system is less than 40 db, the noise will be the primary contributor to the pixel value error, and the digitizer error can be neglected. A signal-to-noise ratio of 40 db (typical of many cameras) is a voltage ratio of 100/1, equivalent to a pixel area error of +/- 1 percent. A description of the centroid and second moment of inertia algorithms, and a determination of overall error of each follows, along with the error of locating the bead from the example above.

1. CENTROID

Figure 7 shows a general case for determining the centroid of an area relative to a set of orthogonal axes, labeled x and y:
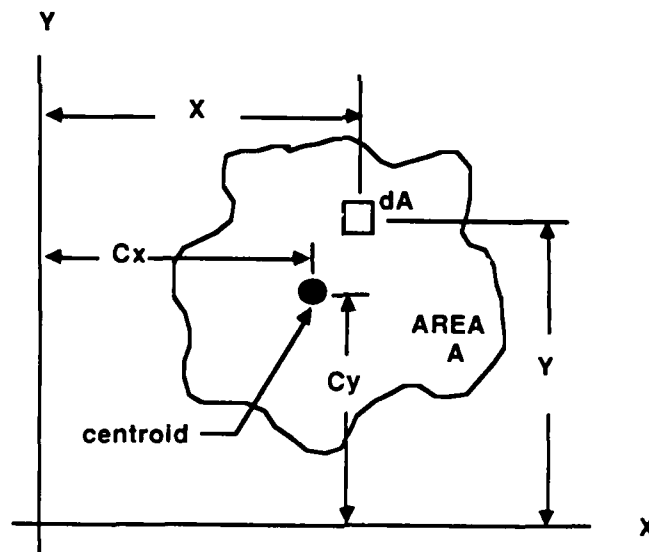
Figure 7. Centroid of an Area

The equations (Reference 4) for the centroid of the area A are given by:

$$C_x = \frac{\int X f_n \, dA}{\int f_n \, dA} = \frac{\sum_{0}^{N} X f_n \Delta A}{\sum_{0}^{N} f_n \Delta A} \qquad (3)$$

$$C_y = \frac{\int Y f_n \, dA}{\int f_n \, dA} = \frac{\sum_{0}^{N} Y f_n \Delta A}{\sum_{0}^{N} f_n \Delta A} \qquad (4)$$

Where ΔA is one pixel area, f_n is the fraction of each pixel area, ΔA, covered and N is the number of pixels. For digital systems, the integral is easily approximated by doing a summation.

If each ΔA is accurate to +/- 1 percent (due to noise contribution), then the sum of ΔAs for 17 pixels (bead example with a 2048 x 1024 array) is accurate to +/- 0.24 percent, assuming noncorrelated noise, since we get the statistical improvement of $\frac{1}{\sqrt{N}}$ where N = 17. The location accuracy of 0.24 percent within a pixel dimension of 1.19 mm yields 0.0029 mm (0.0001") accuracy, or about two orders of magnitude improvement over the +/- 0.5 pixel or 50 percent accuracy computed earlier for locating a point. Therefore, we see that the centroid method of locating an object is more accurate than just locating a point on the object, provided N>1.

2. SECOND MOMENT OF INERTIA OF AN AREA

Figure 8 shows a general case for determining the second moment of inertia of an area with respect to the centroid of the area. It turns out that finding the second moment with respect to the centroid rather than to arbitrary axes is simpler because the arbitrary axes moment terms do not have to be carried through the equations.
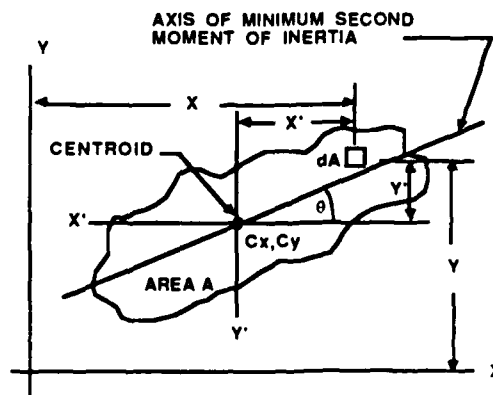
Figure 8. Second Moment of Inertia of an Area

11

The equation (Reference 4) for the angle of the axis through the centroid of the second moment of inertia of an area is:

$$\text{TAN } 2\theta = \frac{-2P_c}{I_x - I_y} \qquad (5)$$

Where: $I_y = \int x'^2 dA$ (second moment with respect to y axis)

$I_x = \int y'^2 dA$ (second moment with respect to x axis)

$P_c = \int x'y' dA$ (product of inertia)

and θ = Angle of the axis of the second moment of inertia relative to the x' axis.

x' = Distance from the centroid to dA in the x direction.

y' = Distance from the centroid to dA in the y direction.

Note that the result yields two axes 90° apart, being the maximum and minimum axes of the second moment of inertia of the area A. For our purposes, we are only interested in the axis of the minimum second moment.

One might intuitively surmise that finding the angle of the second moment of inertia of an area is more accurate than the geometric solution due to the statistical improvement of using more data points. There is some additional help due to the fact that only pixels on the edge of the area are affected by noise. Interior pixels are known to be completely covered by the image, and so their values can be corrected (by image processing) to the full value of 1.0.

Rather than undertake an error analysis of the second moment of inertia for random, uncorrelated noise on edge pixels, a simulation was used to prove the accuracy of the technique.

3. CENTROID/SECOND MOMENT OF INERTIA SIMULATION

Using the equations for the centroid and second moment of inertia of an area, a general case problem was created to simulate a real condition to demonstrate the accuracy of the method. A simulation program was written to solve for the second moment axis and use randomly generated "noise" to affect the edge areas of the projectile. This allowed us to determine the effects of random errors on the ΔA values, and also to compute the standard deviation of our calculations, giving us a feel for the accuracy we might expect from the second moment method.

a. Array Size

An array size of 512_v x 256_h was chosen because it was close to optimum for maximum size/cost for available CCD cameras, at the time of the simulation.

b. Projectile Shape

The projectiles generally used at Eglin are bullets, bombs, and shapes that fly well without tumbling as they travel downrange. These are generally oblong shapes with the length much greater than the diameter. Also, the shapes tend to be symmetrical about the long (horizontal) axis. To make matters simple for the drawings and simulation area calculations, a bullet shape of 80 mm long by 20 mm diameter was chosen, because this is the the smallest projectile used at the range. This casts a shadow whose area is easy to calculate. For the simulation, the projectile was drawn at an angle of 20 degrees relative to a horizontal axis (X).

c. Geometric Model

The representative model used is shown in Figure 9 with each small square representing one pixel of the imaging array. All units of measure are in pixel units.
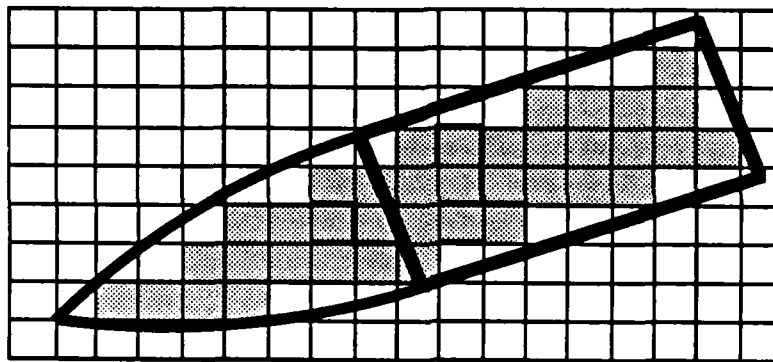
Figure 9. Simulation Model

The size of the projectile at the reflective screen was then mapped onto the 512_v x 256_h array using a spatial resolution factor of the field of view of 1219.2 mm horizontal ÷ 256 horizontal pixels = 4.76 mm per pixel (same for the vertical dimension). The size of the model in pixel units is 16.8 pixels long by 4.2 pixels high. The model was angled at 20 degrees relative to the horizontal.

The interpretation of the shadowgraph of the model overlaying the array is that it simulates the image of the projectile cast on a CCD array. The CCD array provides an output to the imaging system that digitizes to 12 bits with values between 0.0 and 1.0. Pixels fully covered by the shadow will have a value of 1.0 in the system with no noise or error because we know they are interior to the shadow. These are the pixels shown shaded in Figure 9. The pixels that are only partially covered by the shadow (edge pixels) will output a value between 0.0 and 1.0, with random noise added to the ideal value. The noise is a random value between 0 and +/- the reciprocal of the signal to noise ratio (S/N). These are the white portions of pixels shown in Figure 9 that are inside the model shadow outline. The ideal value of each pixel output is proportional to the pixel area subtended by the shadow. To achieve a perfect shadowgraph

13

model, the values for all pixels were read manually from Figure 9, by estimating the number of subareas on a finer gridded graph paper. These areas were used in the simulator as the baseline data for pixel areas. The areas determined manually for all pixels were entered in the simulator for the following calculations, with random noise then added to each pixel area.

d. Simulation Results

The parameters calculated from the "perfect" shadow with no noise added are:

Total Area = 59.171, C_x = 10.020, C_y = 3.562, θ = 19.963 °

Table 1 shows the average values produced by the simulator with noise for the Area, Cx, Cy, angle θ, standard deviation of angle θ, and the 3σ value for angle θ. The value for σ should be used as the probable error to be compared with the current probable error values for the range using the film cameras.

The S/N ratio is calculated using the root-mean-square (RMS) value of the random noise generated, which is a continuous function, and using the voltage ratio of the signal and noise. The signal range is 0 - 1 volt. For each S/N ratio, the simulator was run 25 times to provide a good statistical sample. The standard deviation is based on these 25 runs.

TABLE 1. SIMULATION RESULTS VS. S/N

S/N	Cx	Cy	θ	σ	3σ
3.5	10.031	3.573	19.082	0.7931	2.3793
5.2	10.007	3.560	19.995	0.5614	1.6842
6.9	10.055	3.567	19.782	0.4198	1.2594
8.7	10.021	3.557	19.879	0.3596	1.0788
10.4	9.991	3.554	20.054	0.2658	0.7974
12.1	10.011	3.559	19.899	0.2357	0.7071
13.9	10.016	3.564	19.984	0.2389	0.7167
15.6	10.018	3.563	20.001	0.1920	0.5760
17.3	10.017	3.562	19.984	0.1225	0.3675
26.0	10.016	3.561	19.974	0.0992	0.2976
34.7	10.020	3.562	19.950	0.1021	0.3063
52.0	10.016	3.560	19.968	0.0617	0.1851
69.3	10.020	3.562	19.964	0.0399	0.1197
86.7	10.020	3.563	19.967	0.0199	0.0597
121.3	10.021	3.562	19.964	0.0192	0.0576
173.3	10.020	3.563	19.969	0.0172	0.0516

14

Figure 10 shows a plot of the 3σ angle θ error vs S/N taken from Table 1. It also shows equivalent plots for 5 and 10 degree angles, showing insensitivity to model orientation.
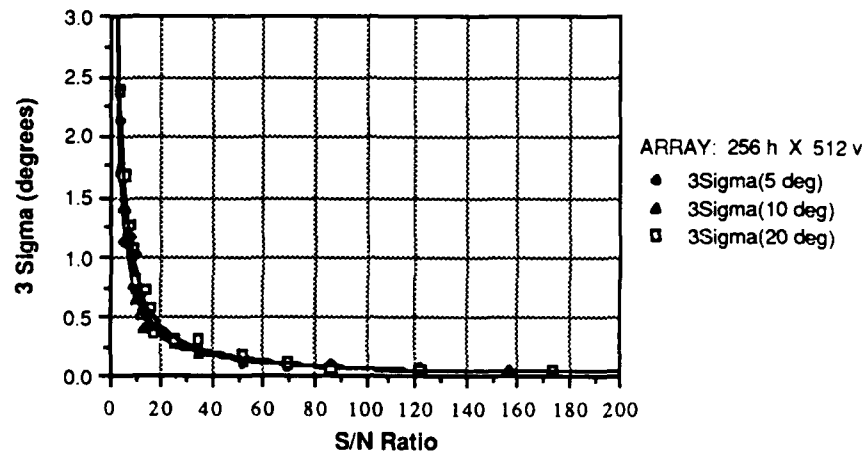
Figure 10.   3σ Angle θ Error vs. S/N

e.   **Error vs. Array Size**

Next, in order to look at the effects of array size on the angular error, the simulator was modified to accommodate various array sizes. Simulations were run for 2048 x 1024, 1024 x 512, and 512 x 256, as the three most likely array sizes to be used. Figure 11 shows the angular error (3σ) vs. S/N for the three array sizes. These plots assumed random noise over the entire projectile image, so the errors in general are higher than that calculated in paragraph V.3.d above.
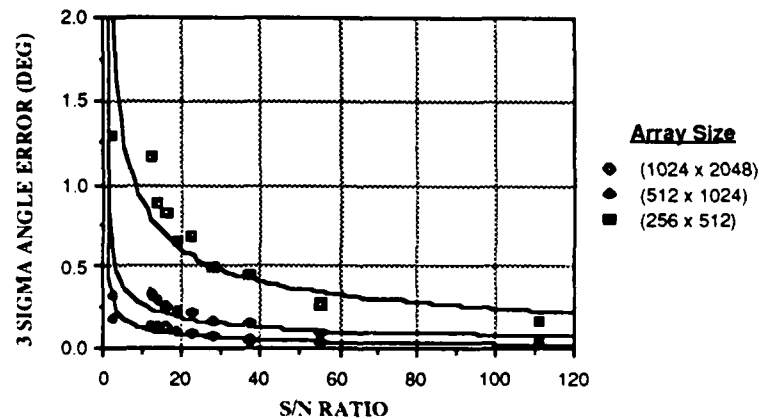
Figure 11.   Angle Error vs. S/N for Various Arrays

15

f. Comparison With the Film Method

The Los Alamos National Laboratory report #LA-10072-MS (Reference 5), contains an analysis of the Eglin Aeroballistics Research Facility. This analysis shows that the resolution capability of the film camera system used at the Aeroballistics Facility has a limiting resolution of 0.72 line pair/millimeter at the screen. This is 1.39 mm/line pair or 0.69 mm/line. This means that an object 0.69 mm wide can just be discriminated, or 0.69 mm is the "error limit" of the Eglin film system. Using that number for the error dimension for locating a point on each end of a line, and using a length of 80 mm for the shortest projectile, we can calculate the error in finding the angle of a line on film by using Equation 1. The calculation is shown in Equation 6.

$$\beta = SIN^{-1} \frac{Error\ Limit}{Length} = SIN^{-1} \frac{0.69\ mm}{80\ mm} = 0.494\ degrees \qquad (6)$$

The β error of 0.494 degrees is based on the assumption that an operator can locate the end points of the line perfectly, resulting in +/- one error limit of resolution. The error for a digital imaging system with an array of 2048_v x 1024_h resolution was shown to be +/- 0.852 degrees with no operator error in locating the end points of the line. The error would be three times that, or +/- 2.56 degrees if there were a +/- 1 pixel error in finding the line end points. Similarly for the film system, with +/- 1 error limit in mislocating the end points of the line, a 1.48 degree error would result.

By comparison, a 512_v x 256_h array with a S/N of 20, which is realizable with the Eglin reflective screen and typical CCD cameras, will yield an angular error of about 0.40 degrees. It can be seen, then, that using the second moment of inertia algorithm with a 512_v x 256_h CCD array will yield angular accuracies of about what the present film system can, and more than twice the accuracy of a 2048_v x 1024_h array camera using the geometric method. A 1024_v x 512_h array camera then will yield angular determinations better than the film system.

SECTION VI

LOCATING A MODEL IN 3-SPACE

By calculating the centroid to locate an object and the second moment of inertia to determine the orientation of the object, the location and orientation can be determined with much greater accuracy than by using geometric methods utilizing only one or two points.

This section details the algorithms, equations, and terminology for determining the orientation of a projectile model and the location of the center of mass, C_G, of the model in 3-space from the centroid and second moment of inertia data from two orthogonal electronically imaged point projections taken in the Eglin Aeroballistics Research Facility configuration.

1. GIVEN INFORMATION

a. The Eglin Aeroballistics Range configuration is shown in Figure 12.

b. The model is symmetric about its principal (horizontal) axis.

c. The model is imaged on orthogonal Hall (side view) and Pit (vertical view) screens by point flash sources at F_H and F_P, with coordinate locations (X_{FH}, Y_{FH}, Z_{FH}) and (X_{FP}, Y_{FP}, Z_{FP}) known.

d. The electronic imaging cameras have detector array sizes of 1024_v x 512_h pixels.

e. The screen size (field of view) to be imaged is 243.84 cm (96") high x 121.92 cm (48") wide.

f. The lower-right calibration bead, B_{1H1}, of the Hall view at window 1 is at range coordinate system location (0,0,0) for X, Y, Z.

g. The range coordinate system has the X-axis downrange, not necessarily through B_{2H1}, the Y-axis crossrange, and the Z-axis vertical. All coordinates are given in centimeters and are referenced to this coordinate system.

h. The center of mass, C_G, as well as the length, diameter, and centroid of the side view cross-sectional area are known.

Figure 12. Eglin Aeroballistics Range Imaging References

2. FIND

a. Calculate the position of the model based on the locations, X_{CG}, Y_{CG}, Z_{CG} of its center of mass, C_G, in 3-space at the station used.

b. Calculate the orientation of the principal axis of the model, in 3-space, by the direction cosines (Reference 6) COS α_M, COS β_M, COS γ_M, of the model's principal axis, relative to the three range coordinate axes.

3. DEFINITIONS

The following designations (Table 2) will be used as reference terms in the descriptions and equations in this report. Designations may be used in combination Example: C_{SH} refers to the (C)entroid of the (S)hadowgraph of the (H)all view.

TABLE 2. REFERENCE DESIGNATIONS

	R	= Spatial resolution of image (cm)
	S	= Shadowgraph image formed on the Hall or Pit screen
	C	= Centroid
*	B	= Bead
	θ_{SH}, θ_{SP}	= Angle of Hall or Pit shadowgraph relative to range X axis
	$\theta_{ISH}, \theta_{ISP}$	= Angle of Hall or Pit shadowgraph relative to image h axis
	$\theta'_{ISH}, \theta'_{ISP}$	= Angle of Hall or Pit shadowgraph relative to image h' axis
	H	= Hall (view on wall of range)
	P	= Pit (view on ceiling of range)
	I	= Image
*	F	= Flash strobe (This is a point light source)
	A	= Point calculated where the axis of the minimum second moment of inertia of the screen projection intersects the Z axis in the Hall view, or the Y' axis in the pit view
*	M_L	= Model length (cm)
*	M_D	= Model diameter (cm)
*	M_{CG}	= Model center of mass relative to the front of the model (cm)
	M_C	= Model centroid relative to the front of the model (cm)
*	E	= Coordinates of inside edge of bead
	a,b,c	= Direction numbers of a line in 3-space, in X, Y, Z directions
	α, β, γ	= Direction angles from the X, Y, Z axes to a line in 3-space
*		= Known quantity, both location and physical dimensions

4. COORDINATE SYSTEMS

There are four reference coordinate systems used in the calculations for determining the location of the model from two orthogonal digital images.

a. Image Coordinate System (h,v)

Image calculations are all done relative to the image coordinate system provided by the image processing software (Reference 7) running on an IBM PC/AT computer. The image coordinate system is shown in Figure 13.
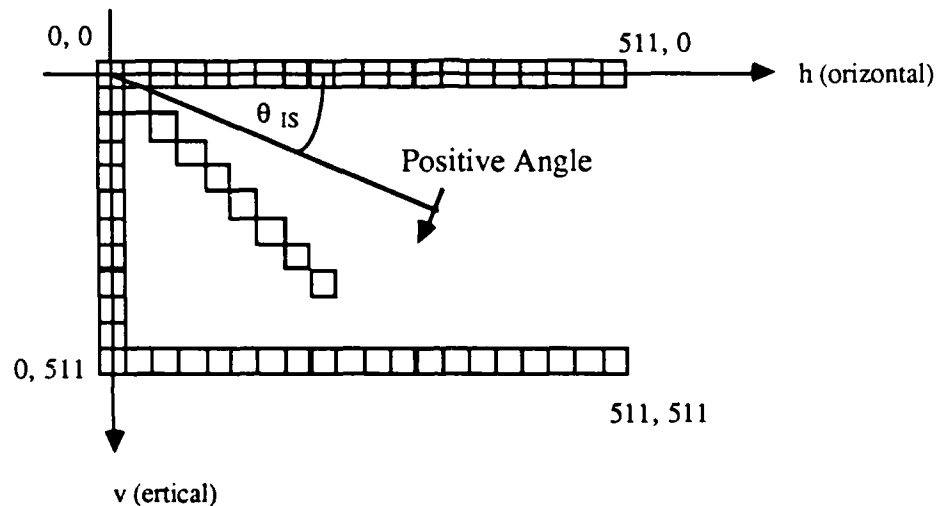
Figure 13. Image Memory Pixel Address References

The h axis is positive to the right and the v axis is positive down. All dimensions are in pixels. The coordinate location, h = 0, v = 0, is in the center of the upper left pixel of the camera, which images a point on the upper left of the shadowgraph screen when viewed from the camera position. The image coordinate range is 512 pixels in both the h and v directions, although the image viewed on the monitor is 512_h x 480_v. This represents only a portion of the 1024_v x 512_h image. A more powerful image processing system is required to process the full 1024_v x 512_h image. The image coordinate system is not necessarily parallel to any other coordinate system.

20

b. Bead Coordinate System in the Image (h', v')

The bead coordinate system is formed in the image by placing the h' axis through the centroids of beads B_1 and B_2 (C_{IB1} and C_{IB2} in Figure 14). The vertical axis is perpendicular to h' and has its origin at C_{IB1}. They are designated h', v' as shown in Figure 14. The dimensions are in pixels. This bead coordinate system is not necessarily parallel to any other coordinate system.
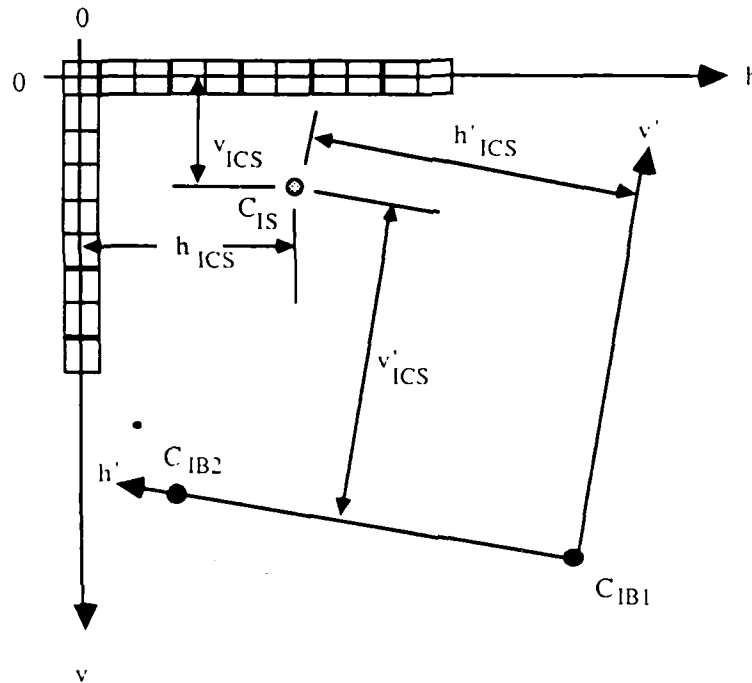
Figure 14. Bead Coordinates in Image

c. Range Coordinate System (X, Y, Z)

The range coordinate system is designated X, Y, Z and is shown in Figure 12. The dimensions are in cm. Location (0,0,0) is at the inside edge (not the centroid) of bead B_{1H1} labeled point E in Figure 6. The X axis is downrange and is parallel to a water level system in the range. The Y axis is crossrange and is also parallel to the water level. The Z axis is vertical and perpendicular to the X and Y axes.

d. Station Coordinate System on the Image (X', Y', Z')

A two-dimensional station coordinate system, parallel to the range coordinate system, is constructed on a Hall or Pit image to allow transforming image coordinates into range coordinates. Figure 16 shows the station coordinate system, designated X'_H, Z'_H, in the Hall view, and X'_P, Z'_P, in the pit view (Q' represents either Z'_H or Z'_P). The origin of each is at the centroid of bead B_1. These station coordinate axes are simply offset from the range axes by constants, which are known, because the locations of the beads in the range are known.

5. IMAGE CALCULATIONS

The image calculations will produce the centroid, C_{IS}, of the shadowgraph of the model. A subscript "I" is used to denote references to image calculations, relative to either the h,v or h',v' axes. A '(prime) is used to distinguish between the h,v axes and the h',v' axes. The centroid units are in pixels in the h,v directions. Also produced is the minimum second moment of inertia, θ_{IS}, through the centroid of the shadowgraph, created by illuminating the model from a point light source, as shown in Figure 12. The angle, θ_{IS}, of the second moment axis relative to the h axis is positive in the positive v direction, so that 0° lies parallel to the h axis and $+90^\circ$ is down, parallel to the v axis (Figure 13). Then the centroids and second moments are translated to the bead reference axes, preparatory for transformation to the range coordinate system.

a. Hall Shadowgraph Image Calculations

(1) Calculate the centroid, C_{IB1H} (h_{ICB1H}, v_{ICB1H}), of bead B_{1H} and the centroid, C_{IB2H} (h_{ICB2H}, v_{ICB2H}), of bead B_{2H}.

(2) Calculate the centroid, C_{ISH} (h_{ICSH}, v_{ICSH}), of the shadowgraph of the model on the Hall screen.

(3) Calculate the angle, θ_{ISH} (degrees), of the minimum second moment of inertia of the shadowgraph area, through the centroid C_{ISH}, relative to the h_H axis.

b. Pit Shadowgraph Image Calculations

(1) Calculate the centroid, C_{IB1P} (h_{ICB1P}, v_{ICB1P}), of bead B_{1P} and the centroid, C_{IB2P} (h_{ICB2P}, v_{ICB2P}), of bead B_{2P}.

(2) Calculate the centroid, C_{ISP} (h_{ICSP}, v_{ICSP}), of the shadowgraph of the model on the Pit screen.

(3) Calculate the angle, θ_{ISP} (degrees), of the minimum second moment of inertia of the shadowgraph area, through the centroid C_{ISP}, relative to the h_P axis.

c. Transform Image Coordinates to the Image Bead Coordinate System

Figure 15 shows the bead coordinate axes, h', v', relative to the image axes, h,v. The transformation can be derived once to apply to both the Hall and Pit images, with all dimensions in pixels. To obtain equations for the Hall, add the subscript $_H$; for the Pit, add the subscript $_P$. The points and angles to be transformed, which are calculated by the centroid and second moment of inertia methods, are indicated as follows to simplify the notation for the derivation of all coordinate transformations:

Point 1   = Centroid of Bead B_1
Point 2   = Centroid of Bead B_2
Point 3   = Centroid of projectile shadowgraph
θ_I = Angle of minimum second moment of inertia of shadowgraph relative to h
θ'_I = Angle of minimum second moment of inertia of shadowgraph relative to h'

22
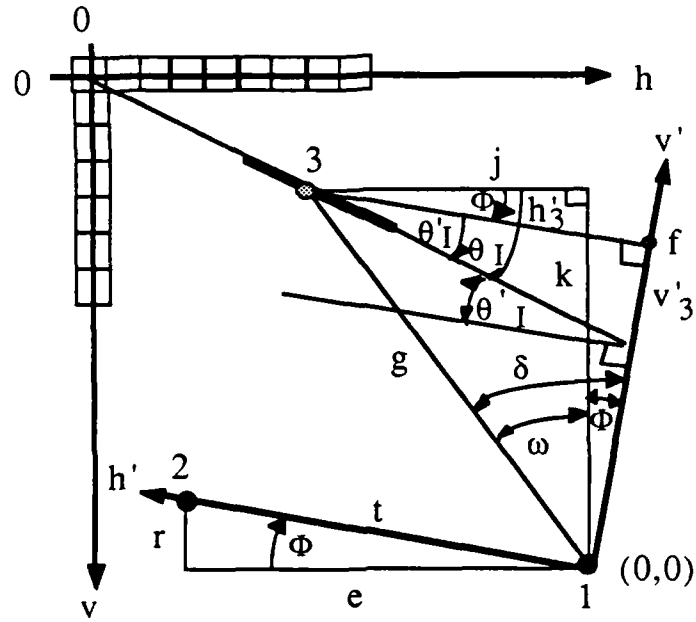
Figure 15. Image to Bead Axis Transformation

Locations of the points in the image, relative to the h,v axes, are designated:

$$\text{Point 1} = h_1, v_1 = C_{IB1} = h_{ICB1}, v_{ICB1} \tag{7}$$

$$\text{Point 2} = h_2, v_2 = C_{IB2} = h_{ICB2}, v_{ICB2} \tag{8}$$

$$\text{Point 3} = h_3, v_3 = C_{IS} = h_{ICS}, v_{ICS} \tag{9}$$

(1) Locate the Bead Coordinate System in the Image

First, the h' axis is drawn through Point 1 and Point 2 with the origin located at Point 1, as shown in Figure 15. Then the v' axis is constructed perpendicular to the h' axis, with its origin at Point 1. Point 1 will now become the origin (0,0)' for the h',v' axes. The dimensions of both the h,v and h',v' axes are in pixels.

(2) Compute the Angle Φ

The angle Φ represents the rotation between the h,v and h',v' axes and is formed by the h' axis and a line through Point 1, parallel to the h axis. The triangle formed with sides r, e, t is used to find the angle Φ which is positive in the direction shown. Sides r and e are calculated from the locations of Points 1 and 2, which are:

$$r = v_1 - v_2 \tag{10}$$

$$e = h_1 - h_2 \tag{11}$$

23

Then the angle, Φ, is given by:

$$\Phi = TAN^{-1} \frac{r}{e} = TAN^{-1} \frac{v_1 - v_2}{h_1 - h_1} \tag{12}$$

(3) Transform the Image Points

Because the centroids for Points 1, 2, 3 have been calculated in paragraph VI.5.a - VI.5.b, equations for the following lines (magnitude) and angles in Figure 15 are:

$$j = h_1 - h_3 \tag{13}$$

$$k = v_1 - v_3 \tag{14}$$

$$g = \sqrt{j^2 + k^2} \tag{15}$$

$$t = \sqrt{r^2 + e^2} \tag{16}$$

$$\omega = TAN^{-1} \frac{j}{k} \tag{17}$$

$$\delta = \omega + \Phi = TAN^{-1} \frac{j}{k} + TAN^{-1} \frac{r}{e} \tag{18}$$

So the locations of Points 1, 2, 3 and angle θ'_1 in the bead coordinate system (h',v') are:

Point 1: $h'_1, v'_1 \quad = (0, 0) \quad$ (by definition) $\tag{19}$

Point 1: $h'_2, v'_2 \quad = (t, 0) \tag{20}$

Point 3: $h'_3, v'_3 \quad = (g\ SIN\ \delta,\ g\ COS\ \delta) \tag{21}$

$\theta'_I \qquad = \theta_I - \Phi \tag{22}$

d. Transform the Bead Coordinate System to Station Coordinate System

The equations for the station coordinate system can be derived once, using station axes X', Q', where Q' is a dummy variable to be replaced by either Z' for the Hall station or Y' for the Pit station in the final equations. Likewise, Q is a dummy variable used with X when referring to a range plane, which is either the X, Z plane or the X, Y plane. Axis Q will be replaced by Z or Y when writing final equations for the Hall or Pit.

(1) Transform Bead Coordinates to Station Coordinates

Figure 16 shows the reference axes X', Q' drawn in the same view as the h',v' axes. The station axis X' has its origin at the centroid of Bead B_1, and is parallel to the range X axis. The station Q' axis is parallel to either the range Y or Z axis, with its origin at the same location as X'. Point locations are:

Point 1 = Centroid of Bead B1
Point 2 = Centroid of Bead B2
Point 3 = Centroid of projectile shadowgraph
Point 4 = Intersection of second moment of inertia of shadowgraph with Q' axis
           (This is called Point A_S in later sections)
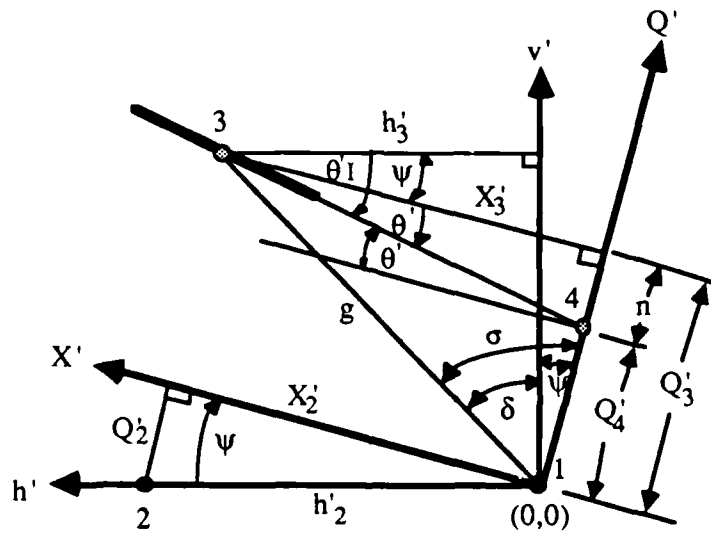
Figure 16. Bead to Station Axis Transformation

The origin of axes X', Q' lies on the origin of h', v' in the image. The dimensions of the X', Q' axes are in pixels, and can be converted easily to centimeters by knowing the spatial resolution of the image.

(2) Compute the Angle ψ

The angle ψ is the rotation angle between the h',v' and X', Q' axes. The range coordinates for the edges of the beads are known as:

$$\text{Edge of Bead } B_1 = X_{EB1}, Y_{EB1}, Z_{EB1} \tag{23}$$
$$\text{Edge of Bead } B_2 = X_{EB2}, Y_{EB2}, Z_{EB2} \tag{24}$$

and the distance from the edge of the bead to its centroid is shown in Figure 6 and is measured as

$$d_B = 0.2728 \text{ cm} \tag{25}$$

25

Figure 17 shows the arrangement of the beads in both the Hall and Pit views and the relationship of the centroids of the beads to the inside edges, which are known in the range coordinate system.
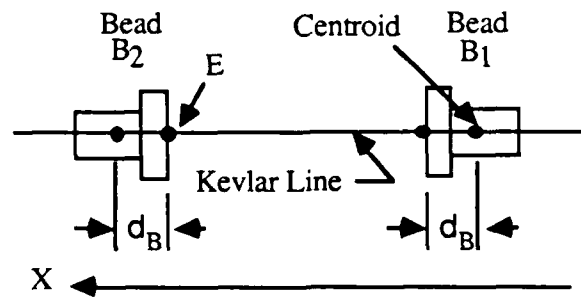
Figure 17. Bead Locations in Hall and Pit Views

Then the approximate range coordinates of the centroid of the beads are:

$$C_{B1} = (X_{EB1} - d_B), Y_{EB1}, Z_{EB1} = X_1, Y_1, Z_1 \qquad (26)$$

$$C_{B2} = (X_{EB2} + d_B), Y_{EB2}, Z_{EB2} = X_2, Y_2, Z_2 \qquad (27)$$

Equations 26 and 27 are not exact if there is appreciable sag in the kevlar line connecting the two beads. But until further investigation, these equations will be used for now.

Since the X, Q and X', Q' axes are parallel, the X, Q range coordinates for Points 1 and 2 can be used to compute the rotation angle, ψ, as shown in Figure 18.
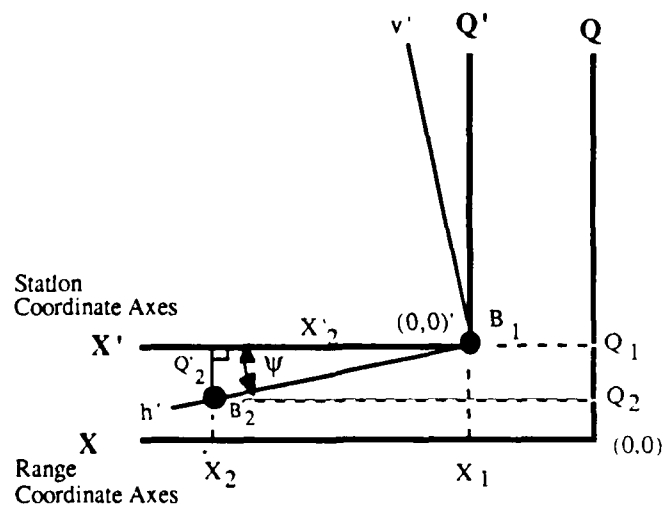
Figure 18. Rotation Angle Calculation

The location of Point 2 in station coordinates, X', Q', is:

$$X'_{2(cm)} = X_2 - X_1 \ (cm) \tag{28}$$

$$Q'_{2(cm)} = Q_2 - Q_1 \ (cm) \tag{29}$$

So the rotation angle ψ is:

$$\psi = TAN^{-1} \frac{Q'_2}{X'_2} = TAN^{-1} \frac{Q_2 - Q_1}{X_2 - X_1} \tag{30}$$

(3) Transform Image Points to Station Coordinate System (X', Q')

By definition, the location of Point 1, with respect to to X', Q' is:

$$X'_1, Q'_1 = (0, 0) \tag{31}$$

Knowing the angle ψ, we can locate Point 2, in pixels, with respect to X', Q' as:

$$X'_2 = h'_2 \ COS \ \psi \tag{32}$$

$$Q'_2 = h'_2 \ SIN \ \psi \tag{33}$$

The angle δ is shown in Equation 18. From Figure 16, angle σ is:

$$\sigma = (\delta + \psi) \tag{34}$$

Then the location of Point 3 can be calculated from the triangle formed by sides g, X'$_3$, Q'$_3$, where g has been calculated in Equation 15. Point 3 is:

$$X'_3 = g \ SIN \ \sigma \tag{35}$$

$$Q'_3 = g \ COS \ \sigma \tag{36}$$

The angle of the second moment of inertia of the shadowgraph is simply:

$$\theta' = \theta'_I - \psi \tag{37}$$

(4) Locate Point 4 (A$_S$) on the Q' Axis

The location of Point 4 is the intersection of the second moment of inertia of the shadowgraph axis with the Q' axis, so the X'$_4$ dimension is zero, and can be calculated:

$$X'_4 = 0 \ (by \ definition) \tag{38}$$

$$Q'_4 = Q'_3 - n \tag{39}$$

$$n = X'_3 \ TAN \ \theta' \tag{40}$$

So: $$Q'_4 = Q'_3 - X'_3 \ TAN \ \theta' \tag{41}$$

27

(5) Transform Hall Bead Coordinates to Station Coordinates

The equations derived in paragraphs VI.5.d.(1) - VI.5.d.(3) can be written for the Hall image Points 1, 2, 3, 4, by substituting Z'_H for Q' terms:

Point 1: $\quad X'_H = 0$ $\hspace{8cm}$ (42)

$\hspace{3.6cm} Z'_H = 0$ $\hspace{8cm}$ (43)

Point 2: $\quad X'_{2H} = h'_{2H} \cos \psi_H$ $\hspace{6cm}$ (44)

$\hspace{3.6cm} Z'_{2H} = h'_{2H} \sin \psi_H$ $\hspace{6cm}$ (45)

Point 3: $\quad X'_{3H} = g_H \sin \sigma_H$ $\hspace{6.4cm}$ (46)

$\hspace{3.6cm} Z'_{3H} = g_H \cos \sigma_H$ $\hspace{6.4cm}$ (47)

Point 4: $\quad X'_{4H} = 0$ $\hspace{7.8cm}$ (48)

$\hspace{3.6cm} Z'_{4H} = Z'_{3H} - X'_{3H} \tan \theta'_H$ $\hspace{4.8cm}$ (49)

$\text{Line} \quad r_H = v_{1H} - v_{2H}$ $\hspace{6cm}$ (50)

$\text{Line} \quad e_H = h_{1H} - h_{2H}$ $\hspace{6cm}$ (51)

$\text{Line} \quad j_H = h_{1H} - h_{3H}$ $\hspace{6cm}$ (52)

$\text{Line} \quad k_H = v_{1H} - v_{3H}$ $\hspace{6cm}$ (53)

$\text{Line} \quad g_H = \sqrt{j_H^2 + k_H^2}$ $\hspace{5.4cm}$ (54)

$\text{Line} \quad t_H = h'_{2H} = \sqrt{e_H^2 + r_H^2}$ $\hspace{4.6cm}$ (55)

$\text{Angle} \quad \theta'_H = \theta'_{1H} - \psi_H$ $\hspace{5.6cm}$ (56)

$\text{Angle} \quad \sigma_H = (\delta_H + \psi_H)$ $\hspace{5.6cm}$ (57)

$\text{Angle} \quad \delta_H = \omega_H + \Phi_H$ $\hspace{5.6cm}$ (58)

$\text{Angle} \quad \omega_H = \tan^{-1} \dfrac{j_H}{k_H}$ $\hspace{5.2cm}$ (59)

$\text{Angle} \quad \Phi_H = \tan^{-1} \dfrac{r_H}{e_H}$ $\hspace{5.2cm}$ (60)

$\text{Angle} \quad \psi_H = \tan^{-1} \dfrac{Z_{CB2H} - Z_{CB1H}}{X_{CB2H} - X_{CB1H}}$ $\hspace{3.6cm}$ (61)

28

(6) Transform Pit Bead Coordinates to Station Coordinates

The equations derived in paragraphs VI.5.d.(1) - VI.5.d.(3) can be rewritten for the Pit image points 1, 2, 3, 4, by substituting Y'_P for Q' terms:

Point 1: $\qquad X'_P \quad = 0$ $\hfill (62)$

$\qquad\qquad\quad Y'_P \quad = 0$ $\hfill (63)$

Point 2: $\qquad X'_{2P} = h'_{2P} \cos \psi_P$ $\hfill (64)$

$\qquad\qquad\quad Y'_{2P} = h'_{2P} \sin \psi_P$ $\hfill (65)$

Point 3: $\qquad X'_{3P} = g_P \sin \sigma_P$ $\hfill (66)$

$\qquad\qquad\quad Y'_{3P} = g_P \cos \sigma_P$ $\hfill (67)$

Point 4: $\qquad X'_{4P} = 0$ $\hfill (68)$

$\qquad\qquad\quad Y'_{4P} = Y'_{3P} - X'_{3P} \tan \theta'_P$ $\hfill (69)$

Line $\quad r_P \quad = v_{1P} - v_{2P}$ $\hfill (70)$

Line $\quad e_P \quad = h_{1P} - h_{2P}$ $\hfill (71)$

Line $\quad j_P \quad = h_{1P} - h_{3P}$ $\hfill (72)$

Line $\quad k_P \quad = v_{1P} - v_{3P}$ $\hfill (73)$

Line $\quad g_P \quad = \sqrt{j_P^2 + k_P^2}$ $\hfill (74)$

Line $\quad t_P \quad = h'_{2P} = \sqrt{e_P^2 + r_P^2}$ $\hfill (75)$

Angle $\quad \theta'_P \quad = \theta'_{1P} - \psi_P$ $\hfill (76)$

Angle $\quad \sigma_P \quad = (\delta_P + \psi_P)$ $\hfill (77)$

Angle $\quad \delta_P \quad = \omega_P + \Phi_P$ $\hfill (78)$

Angle $\quad \omega_P \quad = \tan^{-1} \dfrac{j_P}{k_P}$ $\hfill (79)$

Angle $\quad \Phi_P \quad = \tan^{-1} \dfrac{r_P}{e_P}$ $\hfill (80)$

Angle $\quad \psi_P \quad = \tan^{-1} \dfrac{Z_{CB2P} - Z_{CB1P}}{X_{CB2P} - X_{CB1P}}$ $\hfill (81)$

e. Transform the Station Coordinates to Range Coordinates

This translation does not involve any geometry, but simply requires multiplying X', Y', Z' locations (in pixels) by the spatial resolution of the Hall or Pit view, and then adding the range location offset to the origin of the X', Y' or X', Z' station views. The range location offset to the origin of the Hall or Pit station is the location of the Bead B_1 centroid in each case.

(1) Calculate the Hall and Pit Station Spatial Resolutions

The spatial resolution, R_I, of any image is defined as:

$$R_I = \frac{distance\ (cm)}{\#\ of\ pixels} \qquad (82)$$

The distance between Bead B_1 and Bead B_2, in pixels, has been calculated in each view as the value $h'_2 = t$ (pixels) in Equation 20. The range distance between beads along the h' axis for the Hall and Pit views is shown in Figure 18 and can be calculated in X, Y, Z units (cm). The Hall and Pit spatial resolutions are calculated as follows:

Hall Spatial Resolution in cm/pixel is:

$$R_H = \frac{h'_{2H}\ (cm)}{h'_{2H}\ (pixels)} \qquad \frac{cm}{pixel} \qquad (83)$$

The value $h'_{2H(pixels)}$ has been calculated as Equation 55. The value for $h'_{2H(cm)}$ is given by:

$$h'_{2H(cm)} = \sqrt{(X'_{2H(cm)})^2 + (Z'_{2H(cm)})^2} \quad (cm) \qquad (84)$$

where $X'_{2H(cm)}$ is from Equation 28 and $Z'_{2H(cm)}$ is from Equation 29, substituting Z' for Q' and Z for Q. Values for X_1, X_2 and Z_1, Z_2 are known.

The pit Spatial Resolution in cm/pixel is:

$$R_P = \frac{h'_{2P}\ (cm)}{h'_{2P}\ (pixels)} \qquad \frac{cm}{pixel} \qquad (85)$$

The value $h'_{2P(pixels)}$ has been calculated from Equation 75. The value for $h'_{2P(cm)}$ is given by:

$$h'_{2H(cm)} = \sqrt{(X'_{2H(cm)})^2 + (Z'_{2H(cm)})^2} \quad (cm) \qquad (86)$$

where $X'_{2P(cm)}$ is from Equation 28 and $Y'_{2P(cm)}$ is from Equation 29, substituting Y' for Q' and Y for Q. Values for X_1, X_2 and Y_1, Y_2 are known.

30

(2) Hall Station to Range Coordinate Transformation

The final equations for the Hall station, in terms of range coordinates, will be obtained by multiplying X'_H, Z'_H coordinates by R_H and adding the range offset to the centroid of Bead B_1. The Hall equations in paragraph VI.5.d.(5) for lines, with dimensions in pixels, and angles are still valid and do not need to be converted. All equations will also show the proper subscripts and designations for the points and angles.

$$C_{B1H} = X_{CB1H}, Y_{CB1H}, Z_{CB1H} = (X_{EB1H} - d_B), Y_{EB1H}, Z_{EB1H} \tag{87}$$

$$C_{B2H} = X_{CB2H}, Y_{CB2H}, Z_{CB2H} = (X_{EB2H} + d_B), Y_{EB2H}, Z_{EB2H} \tag{88}$$

$$X'_{2H(cm)} = (X_{CB2H} - X_{CB1H}) \tag{89}$$

$$Z'_{2H(cm)} = (Z_{CB2H} - Z_{CB1H}) \tag{90}$$

$$r_H = v_{CB1H} - v_{CB2H} \tag{91}$$

$$e_H = h_{CB1H} - h_{CB2H} \tag{92}$$

$$j_H = h_{CB1H} - h_{CSH} \tag{93}$$

$$k_H = v_{CB1H} - v_{CSH} \tag{94}$$

$$g_H = \sqrt{j_H^2 + k_H^2} \tag{95}$$

$$t_H = \sqrt{r_H^2 + e_H^2} \tag{96}$$

$$\omega_H = TAN^{-1} \frac{j_H}{k_H} \tag{97}$$

$$\Phi_H = TAN^{-1} \frac{r_H}{e_H} \tag{98}$$

$$\theta'_{IH} = \theta_{IH} - \Phi_H \tag{99}$$

$$\delta_H = \omega_H + \Phi_H \tag{100}$$

$$\psi_H = TAN^{-1} \frac{Z'_{2H(cm)}}{X'_{2H(cm)}} \tag{101}$$

$$\sigma_H = \delta_H + \psi_H \tag{102}$$

$$\theta'_H = \theta'_{IH} + \psi_H \tag{103}$$

31

But $\theta_{SH} = \theta'_H$ since the X and X' axes are parallel, so:

$$\theta_{SH} = \theta_{IH} - \Phi_H - \psi_H \tag{104}$$

$$C_{SH}: \quad X_{CSH} = R_H (g_H \, SIN \, \sigma_H) + X_{CB1H} \tag{105}$$

$$Y_{CSH} = Y_{CB1H} \tag{106}$$

$$Z_{CSH} = R_H (g_H \, COS \, \sigma_H) + Z_{CB1H} \tag{107}$$

$$A_{SH}: \quad X_{ASH} = X_{CB1H} \tag{108}$$

$$Y_{ASH} = Y_{CB1H} \tag{109}$$

$$Z_{ASH} = (Z_{CSH} - X_{CSH} \, TAN \, \theta_{SH}) + Z_{CB1H} \tag{110}$$

(3) Pit Station to Range Coordinate Transformation

The final equations for the Pit station, in terms of range coordinates, will be obtained by multiplying X'_P, Y'_P coordinates by R_P and by adding the range offset to the centroid of Bead B_1. The Pit equations in paragraph VI.5.d.(6) for lines, with dimensions in pixels, and angles are still valid and do not need to be converted. All equations will also show the proper subscripts and designations for the points and angles.

$$C_{B1P} = X_{CB1P}, Y_{CB1P}, Z_{CB1P} = (X_{EB1P} - d_B), Y_{EB1P}, Z_{EB1P} \tag{111}$$

$$C_{B2P} = X_{CB2P}, Y_{CB2P}, Z_{CB2P} = (X_{EB2P} + d_B), Y_{EB2P}, Z_{EB2P} \tag{112}$$

$$X'_{2P(cm)} = (X_{CB2P} - X_{CB1P}) \tag{113}$$

$$Z'_{2P(cm)} = (Z_{CB2P} - Z_{CB1P}) \tag{114}$$

$$r_P = v_{CB1P} - v_{CB2P} \tag{115}$$

$$e_P = h_{CB1P} - h_{CB2P} \tag{116}$$

$$j_P = h_{CB1P} - h_{CSP} \tag{117}$$

$$k_P = v_{CB1P} - v_{CSP} \tag{118}$$

$$g_P = \sqrt{j_P^2 + k_P^2} \tag{119}$$

$$t_P = \sqrt{r_P^2 + e_P^2} \tag{120}$$

$$\omega_P = TAN^{-1} \frac{j_P}{k_P} \tag{121}$$

32

$$\Phi_P = TAN^{-1}\frac{f_P}{e_P} \tag{122}$$

$$\theta'_{IP} = \theta_{IP} - \Phi_P \tag{123}$$

$$\delta_P = \omega_P + \Phi_P \tag{124}$$

$$\psi_P = TAN^{-1}\frac{Z'_{2P(cm)}}{X'_{2P(cm)}} \tag{125}$$

$$\sigma_P = \delta_P + \psi_P \tag{126}$$

$$\theta'_P = \theta'_{IP} + \psi_P \tag{127}$$

But $\theta_{SP} = \theta'_P$ since the X and X' axes are parallel, so:

$$\theta_{SP} = \theta_{IP} - \Phi_P - \psi_P \tag{128}$$

$$C_{SP}: \quad X_{CSP} = R_P (g_P \, SIN \, \sigma_P) + X_{CB1P} \tag{129}$$

$$Y_{CSP} = R_P (g_P \, COS \, \sigma_P) + Y_{CB1P} \tag{130}$$

$$Z_{CSP} = Z_{CB1P} \tag{131}$$

$$A_{SP}: \quad X_{ASP} = X_{CB1P} \tag{132}$$

$$Y_{ASP} = (Y_{CSP} - X_{CSP} \, TAN \, \theta_{SP}) + Y_{CB1P} \tag{133}$$
$$Z_{ASP} = Z_{CB1P} \tag{134}$$

6. LOCATE THE MODEL

Using the information from the shadowgraphs, the location and orientation of the model, in 3-space, is determined. This is accomplished by constructing a Hall plane$_H$ and a Pit plane$_P$ using the shadowgraph data from paragraph VI.5. These planes are shown in Figure 12. The intersection of the two planes is a line, which is the principal axis of the model.

a. Determine the Planes

(1) Plane Notation

Referring to Figure 12, Plane$_H$ is formed by three points F_H, C_{SH}, A_{SH}. Plane$_P$ is formed by points F_P, C_{SP}, A_{SP}. The points have been defined and calculated in earlier sections.

33

For simplicity sake, all points and angles used in model locating calculations now will be referred to as follows:

F_H = Hall Flash
C_H = Hall shadowgraph centroid
A_H = Hall shadowgraph second moment axis intersection with Z' axis
F_P = Pit Flash
C_P = Pit shadowgraph centroid
A_P = Pit shadowgraph second moment axis intersection with Y' axis

where the locations of the points have been determined as:

$$F_H = X_{FH}, Y_{FH}, Z_{FH} \qquad (135)$$

$$C_H = X_{CSH}, Y_{CSH}, Z_{CSH} \qquad (136)$$

$$A_H = X_{ASH}, Y_{ASH}, Z_{ASH} \qquad (137)$$

$$F_P = X_{FP}, Y_{FP}, Z_{FP} \qquad (138)$$

$$C_P = X_{CSP}, Y_{CSP}, Z_{CSP} \qquad (139)$$

$$A_P = X_{ASP}, Y_{ASP}, Z_{ASP} \qquad (140)$$

The angles calculated using the second moment of inertia method are designated:

$$\theta_H = \theta_{SH} \qquad (141)$$
$$\theta_P = \theta_{SP} \qquad (142)$$

(2) Derive the Plane Equations - Plane$_H$ and Plane$_P$

The two planes intersect along the principal axis of the model. The equation of a plane passing through three points (Reference 6) is given by the form:

$$JX + KY + LZ + M = 0 \qquad (143)$$

where J, K, L, and M are constants and X, Y, Z are point coordinates.

Since each point on the plane must satisfy Equation 143, then three equations from the three points may be written:

$$JX_1 + KY_1 + LZ_1 + M = 0 \qquad (144)$$

$$JX_2 + KY_2 + LZ_2 + M = 0 \qquad (145)$$

$$JX_3 + KY_3 + LZ_3 + M = 0 \qquad (146)$$

34

Solving Equations 144, 145, 146 for the coefficients J, K, L, M yields the determinants:

$$J = \begin{vmatrix} Y_1 & Z_1 & 1 \\ Y2 & Z_2 & 1 \\ Y_3 & Z_3 & 1 \end{vmatrix} \quad (147) \qquad K = - \begin{vmatrix} X_1 & Z_1 & 1 \\ X_2 & Z_2 & 1 \\ X_3 & Z_3 & 1 \end{vmatrix} \quad (148)$$

$$L = \begin{vmatrix} X_1 & Y_1 & 1 \\ X_2 & Y_2 & 1 \\ X_3 & Y_3 & 1 \end{vmatrix} \quad (149) \qquad M = - \begin{vmatrix} X_1 & Y_1 & Z_1 \\ X_2 & Y_2 & Z_2 \\ X_3 & Y_3 & Z_3 \end{vmatrix} \quad (150)$$

If the three points defining $Plane_H$ are F_H, C_H, A_H, and F_P, C_P, A_P define $Plane_P$, then we will let Equation 144 be the equation for point F, Equation 145 represent C, and Equation 146 represent A. Solving the three equations 144, 145, 146 for the coefficients J_H, K_H, L_H, M_H, we obtain the equation for PlaneH, which is:

$$J_H X + K_H Y + L_H Z + M_H = 0 \qquad (151)$$

where the coefficients J_H, K_H, L_H, M_H are defined by the determinants:

$$J_H = \begin{vmatrix} Y_{FH} & Z_{FH} & 1 \\ Y_{CH} & Z_{CH} & 1 \\ Y_{AH} & Z_{AH} & 1 \end{vmatrix} \quad (152) \qquad K_H = - \begin{vmatrix} X_{FH} & Z_{FH} & 1 \\ X_{CH} & Z_{CH} & 1 \\ X_{AH} & Z_{AH} & 1 \end{vmatrix} \quad (153)$$

$$L_H = \begin{vmatrix} X_{FH} & Y_{FH} & 1 \\ X_{CH} & Y_{CH} & 1 \\ X_{AH} & Y_{AH} & 1 \end{vmatrix} \quad (154) \qquad M_H = - \begin{vmatrix} X_{FH} & Y_{FH} & Z_{FH} \\ X_{CH} & Y_{CH} & Z_{CH} \\ X_{AH} & Y_{AH} & Z_{AH} \end{vmatrix} \quad (155)$$

Likewise, solving equations 144, 145, 146 for J_P, K_P, L_P, M_P, the equation for $Plane_P$ is:

$$J_P X + K_P Y + L_P Z + M_P = 0 \qquad (156)$$

where the coefficients J_P, K_P, L_P, M_P are defined by the determinants:

$$J_P = \begin{vmatrix} Y_{FP} & Z_{FP} & 1 \\ Y_{CP} & Z_{CP} & 1 \\ Y_{AP} & Z_{AP} & 1 \end{vmatrix} \quad (157) \qquad K_P = - \begin{vmatrix} X_{FP} & Z_{FP} & 1 \\ X_{CP} & Z_{CP} & 1 \\ X_{AP} & Z_{AP} & 1 \end{vmatrix} \quad (158)$$

$$L_P = \begin{vmatrix} X_{FP} & Y_{FP} & 1 \\ X_{CP} & Y_{CP} & 1 \\ X_{AP} & Y_{AP} & 1 \end{vmatrix} \quad (159) \qquad M_P = - \begin{vmatrix} X_{FP} & Y_{FP} & Z_{FP} \\ X_{CP} & Y_{CP} & Z_{CP} \\ X_{AP} & Y_{AP} & Z_{AP} \end{vmatrix} \quad (160)$$

(3) Compute the Intersection of the Two Planes, Plane$_H$, Plane$_P$.

The intersection of the two planes is a line along the principal axis of the model. The line is described by direction numbers a_M, b_M, c_M, or by the direction cosines COS α_M, COS β_M, COS γ_M.

Using Equations 151 and 156, the direction cosines of the line of intersection of the two planes may be determined. From the intersection of two lines lying in the two planes, we can determine a point on the line of intersection of the two planes. One point and the direction cosines of a line are sufficient to fully describe the line. The point corresponds to the centroid of the side view cross-sectional area of the model, because that is what is determined from the Hall and Pit images. The line corresponds to the principal axis of the model, since that is determined also in the images. The coefficients of X,Y,Z in the equation for a plane are proportional to the direction cosines of a line perpendicular to the plane. Because the line of intersection of two planes must lie in both planes, then it must also be perpendicular to the perpendicular lines of both planes described by their direction cosines. Because the direction cosines of a line are also proportional to the direction numbers of the line, direction numbers may be used to define a line.

The requirement for perpendicularity for two lines (Reference 6) is:

$$a\,a' + b\,b' + c\,c' = 0 \qquad (161)$$

where a,b,c are the direction numbers for one line, and a',b',c' are the direction numbers for the second line.

The coefficients of X, Y, Z from Equations 151 and 156 are J, K, L, and they are proportional to the direction numbers for the line perpendicular to the plane that describes the plane. Substituting the coefficients for Equations 151 and 156 for the direction numbers a',b',c' in the previous equation, two equations result:

$$J_H\, a + K_H\, b + L_H\, c = 0 \qquad (162)$$

$$J_P\, a + K_P\, b + L_P\, c = 0 \qquad (163)$$

Solving Equations 162 and 163 simultaneously results in the equations for the direction numbers a_M, b_M, c_M, for the line of intersection of planes Plane$_H$ and Plane$_P$, which are also the direction numbers for the principal axis through the model:

$$a_M = K_H L_P - K_P L_H \qquad (164)$$

$$b_M = L_H J_P - L_P J_H \qquad (165)$$

$$c_M = J_H K_P - J_P K_H \qquad (166)$$

The values for J_H, K_H, L_H are from Equations 152 through 155, and J_P, K_P, L_P are from Equations 157 through 160, which are defined in terms of known values.

36

From the direction numbers a_M, b_M, c_M, in Equations 164 through 166, the direction cosines of the model principal axis are given by the equations:

$$COS\ \alpha_M = \frac{a_M}{+/-\ \sqrt{a_M^2 + b_M^2 + c_M^2}} \qquad (167)$$

$$COS\ \beta_M = \frac{b_M}{+/-\ \sqrt{a_M^2 + b_M^2 + c_M^2}} \qquad (168)$$

$$COS\ \gamma_M = \frac{c_M}{+/-\ \sqrt{a_M^2 + b_M^2 + c_M^2}} \qquad (169)$$

(4) Find the Centroid, C_M, of the Side View Area of the Model.

The centroid is found as the intersection of the two lines, lying in planes $Plane_H$ and $Plane_P$, which are drawn from the flash F_H to the Hall shadowgraph C_H and from F_P to the pit shadowgraph C_P. Point C_M is located by (X_{CM}, Y_{CM}, Z_{CM}).

To find the intersection of two lines in 3-space, their equations must be known and solved simultaneously. The equations for each line are written as the equations for two intersecting planes, one of which is $Plane_H$ for the Hall and $Plane_P$ for the Pit. Equations for the second describing plane for each line must be derived. The simplest plane in each case will be the projection plane that is perpendicular to the range coordinate plane YZ and contains the line $F_H C_H$ for the Hall and $F_P C_P$ for the Pit. The general equation for a line defined by two points P_1, and P_2, with coordinates X_1, Y_1, Z_1, and X_2, Y_2, Z_2, is :

$$\frac{X - X_1}{X_2 - X_1} = \frac{Y - Y_1}{Y_2 - Y_1} = \frac{Z - Z_1}{Z_2 - Z_1} \qquad (170)$$

and is also defined as:

$$\frac{X - X_1}{a} = \frac{Y - Y_1}{b} = \frac{Z - Z_1}{c} \qquad (171)$$

where a,b,c are the direction numbers for the line. So we can equate:

$$a\quad = X_2 - X_1 \qquad (172)$$

$$b\quad = Y_2 - Y_1 \qquad (173)$$

$$c\quad = Z_2 - Z_1 \qquad (174)$$

37

The equation for a projection plane, perpendicular to the YZ plane and passing through a line, has its X term eliminated, and the general form reduces to:

$$\frac{Y - Y_1}{b} = \frac{Z - Z_1}{c} \tag{175}$$

where Y_1, Z_1 is a point on the line, and b, c are direction numbers for the line in the Y, Z directions. Rewriting the general form into the more familiar equation for a projection plane through a line, with direction numbers a,b,c, onto plane YZ, we obtain:

$$cY - bZ + (bZ_1 - cY_1) = 0 \tag{176}$$

The direction numbers for the lines $F_H C_H$ and $F_P C_P$ are proportional to the points on the line as in Equation 171, so the direction numbers for the Hall and Pit centroid lines are:

$$a_H = X_{CH} - X_{FH} \tag{177}$$
$$a_P = X_{CP} - X_{FP} \tag{178}$$

$$b_H = Y_{CH} - Y_{FH} \tag{179}$$
$$b_P = Y_{CP} - Y_{FP} \tag{180}$$

$$c_H = Z_{CH} - Z_{FH} \tag{181}$$
$$c_P = Z_{CP} - Z_{FP} \tag{182}$$

Substituting Hall and Pit notations into Equation 176 for b, c, we get the two equations for the projecting planes for the Hall and Pit centroid lines:

$$c_H Y - b_H Z + (b_H Z_{CH} - c_H Y_{CH}) = 0 \tag{183}$$

$$c_P Y - b_P Z + (b_P Z_{CP} - c_P Y_{CP}) = 0 \tag{184}$$

Then letting:

$$D_H = b_H Z_{CH} - c_H Y_{CH} \tag{185}$$

$$D_P = b_P Z_{CP} - c_P Y_{CP} \tag{186}$$

we rewrite Equations 183 and 184 into a simpler form:

$$c_H Y - b_H Z + D_H = 0 \tag{187}$$

$$c_P Y - b_P Z + D_P = 0 \tag{188}$$

where Equation 187 is for the projection plane on YZ through line $F_H C_H$ and Equation 188 is for the projection plane on YZ through line $F_P C_P$.

The intersection of lines $F_H C_H$ and $F_P C_P$ can be found by solving the equations for two planes forming $F_H C_H$ and one equation from line $F_P C_P$. This actually is the intersection of line $F_H C_H$ with one plane describing line $F_P C_P$. Therefore, to show that the two lines do intersect, we must also find the intersection of line $F_H C_H$ with the other plane describing line $F_P C_P$. If the coordinates resulting from the intersection of line $F_H C_H$ with the two planes of line $F_P C_P$ are not the same, we will use for now the average value of the two results.

38

We can solve for the intersection of line $F_H C_H$ with $Plane_P$ by solving the equations for line $F_H C_H$ and $Plane_P$ simultaneously.

Line $F_H C_H$ is given by Equations 151 and 187:

$$J_H X + K_H Y + L_H Z + M_H = 0 \tag{151}$$

$$c_H Y - b_H Z + D_H = 0 \tag{187}$$

Line $F_P C_P$ is given by Equations 156 and 188:

$$J_P X + K_P Y + L_P Z + M_P = 0 \tag{156}$$

$$c_P Y - b_P Z + D_P = 0 \tag{188}$$

The general solution to three equations with three unknowns, X,Y,Z from the form:

$$A_1 X + B_1 Y + C_1 Z = D_1 \tag{189}$$

$$A_2 X + B_2 Y + C_2 Z = D_2 \tag{190}$$

$$A_3 X + B_3 Y + C_3 Z = D_3 \tag{191}$$

is given by:

$$X = \frac{\Delta X}{\Delta}, \quad Y = \frac{\Delta Y}{\Delta}, \quad Z = \frac{\Delta Z}{\Delta} \tag{192}$$

where the determinants for the solutions of Δ, ΔX, ΔY, ΔZ are:

$$\Delta = \begin{vmatrix} A_1 & B_1 & C_1 \\ A_2 & B_2 & C_2 \\ A_3 & B_3 & C_3 \end{vmatrix} \tag{193} \qquad \Delta X = \begin{vmatrix} D_1 & B_1 & C_1 \\ D_2 & B_2 & C_2 \\ D_3 & B_3 & C_3 \end{vmatrix} \tag{194}$$

$$\Delta Y = \begin{vmatrix} A_1 & D_1 & C_1 \\ A_2 & D_2 & C_2 \\ A_3 & D_3 & C_3 \end{vmatrix} \tag{195} \qquad \Delta Z = \begin{vmatrix} A_1 & B_1 & D_1 \\ A_2 & B_2 & D_2 \\ A_3 & B_3 & D_3 \end{vmatrix} \tag{196}$$

39

Solving Equations 151, 187, and 156, we get the Δ values, denoted by subscript $_{156}$, for the intersection of line $F_H C_H$ with Plane$_P$ using the general solution to three equations with three unknowns described above:

$$\Delta_{156} = \begin{vmatrix} J_H & K_H & L_H \\ 0 & c_H & -b_H \\ J_P & K_P & L_P \end{vmatrix} \quad (197) \qquad \Delta X_{156} = \begin{vmatrix} -M_H & K_H & L_H \\ -D_H & c_H & -b_H \\ -M_P & K_P & L_P \end{vmatrix} \quad (198)$$

$$\Delta Y_{156} = \begin{vmatrix} J_H & -M_H & L_H \\ 0 & -D_H & -b_H \\ J_P & -M_P & L_P \end{vmatrix} \quad (199) \qquad \Delta Z_{156} = \begin{vmatrix} J_H & K_H & -M_H \\ 0 & c_H & -D_H \\ J_P & K_P & -M_P \end{vmatrix} \quad (200)$$

Likewise, solving Equations 151, 187, and 188, we get the Δ values, denoted by subscript $_{188}$, for the line $F_H C_H$ intersection with the projection plane onto YZ through line $F_P C_P$:

$$\Delta_{188} = \begin{vmatrix} J_H & K_H & L_H \\ 0 & c_H & -b_H \\ 0 & c_P & -b_P \end{vmatrix} \quad (201) \qquad \Delta X_{188} = \begin{vmatrix} -M_H & K_H & L_H \\ -D_H & c_H & -b_H \\ -D_P & c_P & -b_P \end{vmatrix} \quad (202)$$

$$\Delta Y_{188} = \begin{vmatrix} J_H & -M_H & L_H \\ 0 & -D_H & -b_H \\ 0 & -D_P & b_P \end{vmatrix} \quad (203) \qquad \Delta Z_{188} = \begin{vmatrix} J_H & K_H & -M_H \\ 0 & c_H & -D_H \\ 0 & c_P & -D_P \end{vmatrix} \quad (204)$$

Using the solutions for the Δ values from Equations 197 through 200 for the intersection of line $F_H C_H$ and Plane$_P$ (Δ_{156} subscripts) and the solutions for the Δ values from Equations 201 through 204 for the intersection of line $F_H C_H$ and projection plane onto YZ through line $F_P C_P$ (Δ_{188} subscripts), we can write the equations for the coordinates of the centroid of the model:

$$\underline{C_M \text{ on Plane}_P} \qquad\qquad \underline{C_M \text{ on Plane YZ Projection}}$$

$$X_{CM156} = \frac{\Delta X_{156}}{\Delta_{156}} \quad (205) \qquad\qquad X_{CM188} = \frac{\Delta X_{188}}{\Delta_{188}} \quad (208)$$

$$Y_{CM156} = \frac{\Delta Y_{156}}{\Delta_{156}} \quad (206) \qquad\qquad Y_{CM188} = \frac{\Delta Y_{188}}{\Delta_{188}} \quad (209)$$

$$Z_{CM156} = \frac{\Delta Z_{156}}{\Delta_{156}} \quad (207) \qquad\qquad Z_{CM188} = \frac{\Delta Z_{188}}{\Delta_{188}} \quad (210)$$

If the values from Equations 205 through 207 are different from those of Equations 208 through 210, then the values to use for the location of the centroid of the model should be the average of the values. (In reality the centroid point should be half the length of a perpendicular drawn between the closest points of the two lines, but we will use the average for now.)

So the average values for the coordinates of the model centroid C_M are:

$$X_{CM} = \frac{X_{CM156} + X_{CM188}}{2} \tag{211}$$

$$Y_{CM} = \frac{Y_{CM156} + Y_{CM188}}{2} \tag{212}$$

$$Z_{CM} = \frac{Z_{CM156} + Z_{CM188}}{2} \tag{213}$$

The coordinate locations for the center of mass, C_G, of the model are:

$$X_{CG} = X_{CM} + \Delta x \tag{214}$$
$$Y_{CG} = Y_{CM} + \Delta y \tag{215}$$
$$Z_{CG} = Z_{CM} + \Delta z \tag{216}$$

The Δx, Δy, Δz values are related to the distance, d_{CG}, between the centroid and the center of mass along the model axis, which is:

$$d_{CG} = (M_C - M_{CG}) \tag{217}$$

where M_C and M_{CG} are known values obtained from the model. From simple trigonometry, the equations for Δx, Δy, Δz are:

$$\Delta x = d_{CG} \cos \alpha_M \tag{218}$$

$$\Delta y = d_{CG} \cos \beta_M \tag{219}$$

$$\Delta z = d_{CG} \cos \gamma_M \tag{220}$$

Substituting Equations 217 through 220 into Equations 214 through 216, we get the coordinate locations for the center of mass, C_G, of the model:

$$X_{CG} = X_{CM} + d_{CG} \cos \alpha_M \tag{221}$$
$$Y_{CG} = Y_{CM} + d_{CG} \cos \beta_M \tag{222}$$
$$Z_{CG} = Z_{CM} + d_{CG} \cos \gamma_M \tag{223}$$

41

7. COMMENTS

The solutions for the centroid, center of mass, and direction cosines of the principal axis through the model were derived using known constants for the locations of the reference beads in both the Hall and Pit views. The location of Bead B_{1H} does not necessarily have to be the coordinate location (0,0,0), so the equations are general enough to be used for any station along the range.

The location for the C_G of the model is based on the assumption that the C_G and the centroid of the projection of the model lie on the same major axis. If they do not, Equations 221 through 223 must be modified.

The spatial resolution factors determined for the Hall and Pit views are only the horizontal resolutions, determined by the measurement and known distance between beads 1 and 2 in each view. If the vertical resolution is to be used also, the camera measurement of the distance between bead 1 and bead 3 must be used. However, Eglin has found that the vertical and horizontal resolutions are almost always equal.

SECTION VII

PROOF-OF-PRINCIPLE SYSTEM

The proof-of-principle system for high-speed electronic imaging was delivered to the Aeroballistics Research Facility of the Eglin Air Force Base on May 18, 1987.

The purpose of the system was to demonstrate the feasibility of either replacing or augmenting the current film camera system presently operating in the Research Facility with solid state video cameras. This demonstration was to show the measurement resolution capability for locating projectiles as they fly down the range and also to demonstrate proper sensitivity and operation in situ at the range using existing range timing, controls, and spark-gap illumination.

Another purpose of the demonstration was to show the effects of special purpose algorithms and image processing on improving the accuracy of the measured projectile location. The goal was to show the potential of matching the accuracy of the film system.

Primary reasons to replace the film system in the range with electronic imaging is to reduce the time to get test data from 6 to 8 weeks to a few hours, eliminate the installation's dependency on single-source film, and to improve repeatability of measurements.

1. CONFIGURATION

The study detailed in Section V has shown that 1024_v x 512_h resolution electronic imaging cameras have sufficient accuracy, when used with centroid and second-moment-of-inertia algorithms, to yield measurement results comparable to the film system. Based upon that, the proof-of-principle system simulated a 1024_v x 512_h camera system by using zoom lenses on 512 x 512 resolution cameras to reduce the field of view to achieve equal spatial resolution.

The 1024_v x 512_h cameras had to be simulated, because a camera with the right resolution and price was not currently available. The proof-of-principle system was then configured as follows:

    a.   Two GE Model 2250 charge-injection device (CID) Cameras with 12.5 to 75-mm zoom lenses, 512_v x 512_h resolution, single-frame integrate-mode operation.

    b.   Two Poynting Products Model M5250-PC controllers for the GE cameras, interfaced to an IBM PC/AT computer.

    c.   IBM PC/AT computer with 1-mb memory, running PC-DOS vs 3.1, with a monochrome monitor.

    d   Imaging Technology Model FG-100-AT-1024 image processing card, with 1 mb memory. The PC card was installed in the IBM AT.

    e.   Sony 19" color monitor with 512_h x 490_v resolution. The color monitor was connected to the FG-100 PC card.

f. Werner-Frei "Imagelab" image processing software (Reference 7) for the FG-100. This includes a subroutine library "Toolbox" with subroutines usable from Fortran programs.

g. Microsoft Mouse and Mouse driver software. This is a PC card installed in the IBM AT, along with the driver software. The Mouse is used by the Werner-Frei "Imagelab" operating system to select menu commands or areas in an image for processing.

h. Infrared filters installed in the zoom lenses to filter out the IR screen light used at the facility. The filter cutoff is about 700 nm.

2. ASSEMBLY AT LOS ALAMOS

The system was assembled and tested at Los Alamos prior to delivery to Eglin. Additional software was also written to provide some image processing capability not provided by Werner-Frei . The two algorithms (centroid and second-moment-of-inertia) were also coded, along with the equations for locating an object in 3-space from two orthogonal point projections. Software to operate the cameras was also written, and menus for operation were embedded in the "Imagelab" operating system.

The system and software were tested by operating the cameras, processing images, and by calculating the centroids and second-moments-of-inertia of several objects of known size and orientation placed directly in memory (not imaged by a camera). The algorithms and software all seemed to work with very high accuracy.

3. INSTALLATION AT EGLIN

On May 18, 1987, the system was delivered to Eglin. It was unpacked, assembled, and preliminary tests found it to be in good operating order. Mr. R. J. Kelley, manager of the research facility, allocated space and locations for the equipment, and assigned John Krieger, technician, to us to help in the installation. This included running cables, making connections, fabrication of camera and mirror mounts, and connecting the camera system to the range firing control system. Figure 19 shows the IBM AT computer and the Sony color monitor located in the control room at the Aeroballistics Research Facility. Cables were run overhead in cable trays to the cameras in the firing range and to the control console in the same control room.
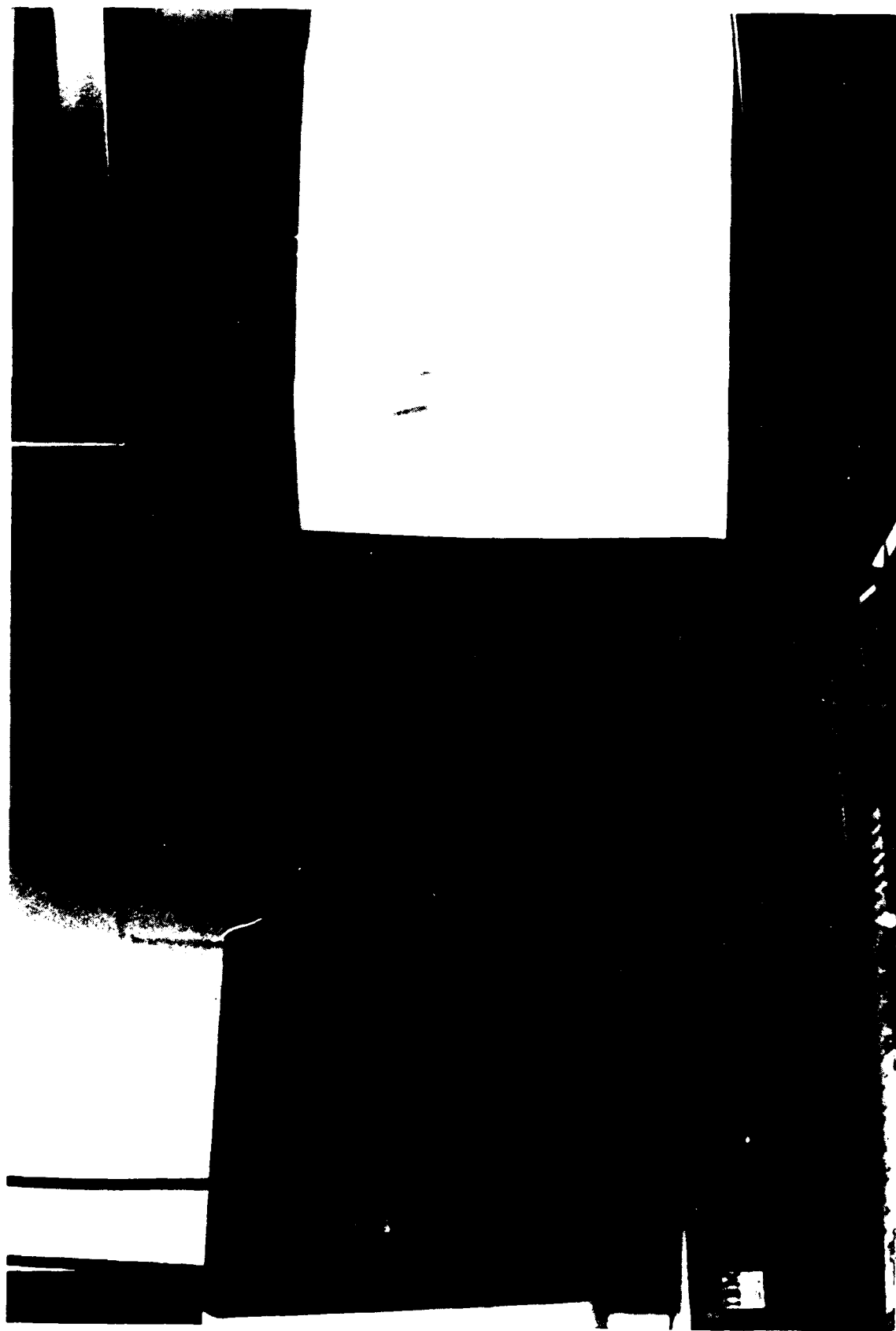
Figure 19. Computer and Image Processor

The Poynting Products camera controllers were located in the Public Address amplifier rack, behind the computer. It should be mentioned that the cables between the cameras and controllers were 100 feet long, a factor which resulted in some degradation of the images. The full-range implementation will have the image buffers in the camera itself, eliminating this long cable run and its resultant noise and loss of resolution.

Figure 20 is a photograph of the Hall camera installation at Station 1. The film camera is at the top, the spark gap is the circle in the center, and the IR screen is at the bottom right of the picture. The GE camera is at the lower center and is mounted closer to the spark gap than the film camera to compensate for the lower CID sensitivity. Tests have shown that the CCD camera is about three lens f-stops more sensitive than the GE CID cameras. This picture shows that the electronic imaging camera can be installed alongside the existing range cameras and equipment without disturbing their installation. This allows the film system to remain intact and operational while the electronic imaging system is installed.

Figure 21 shows the Pit camera installation, which was slightly different from the Hall installation, in that a turning mirror was used because of the different mount configuration for the Pit camera. This causes the image to be backwards, but that was reversed by the computer.

Part of the spark gap can be seen between the film camera and the mirror. The Pit does not have an IR screen, because its spark gap is triggered from the corresponding Hall IR screen.
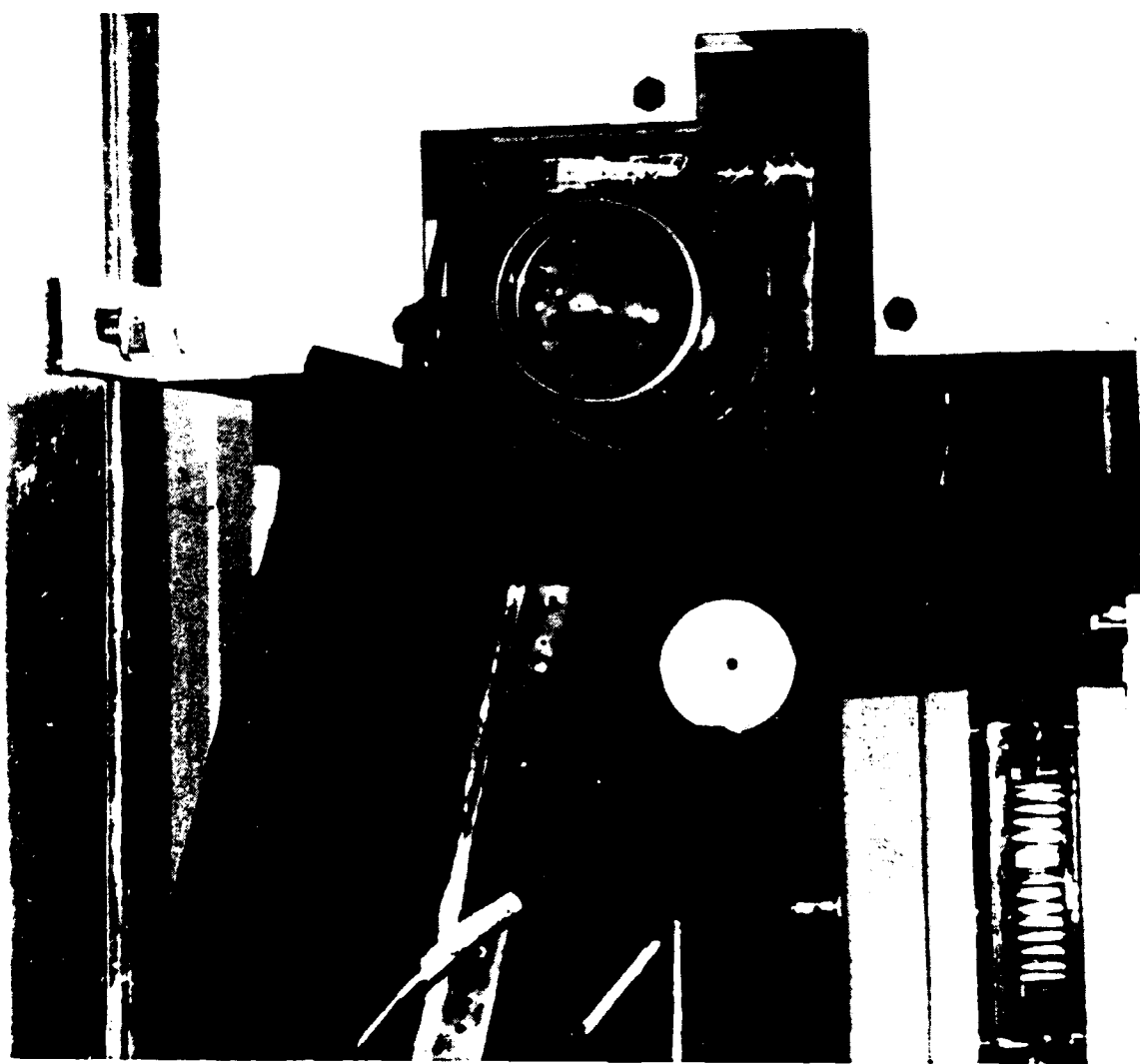
46

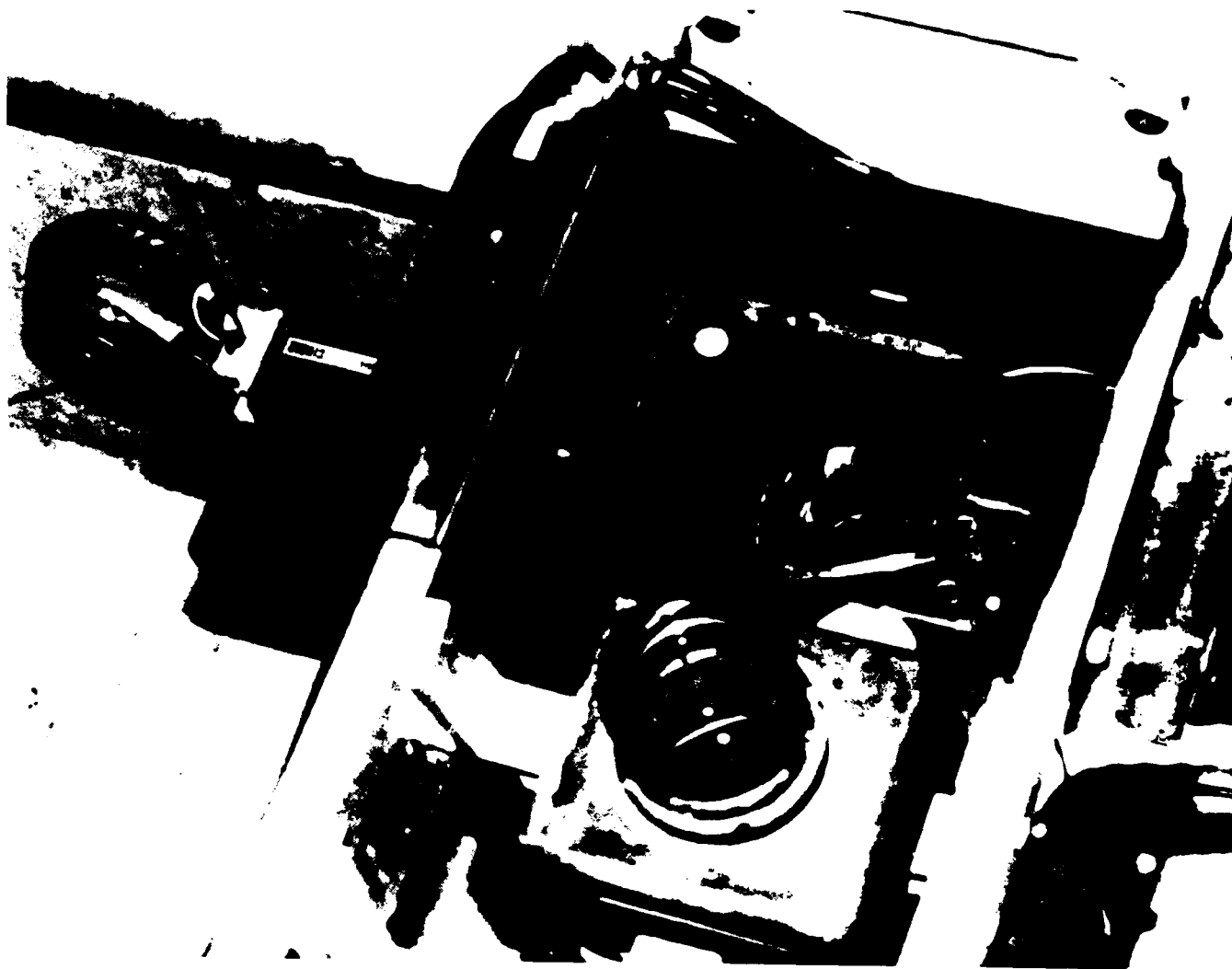Figure 20. Hall Camera Installation

Figure 21. Pit Camera Installation

4. CONTROLS AND OPERATION

Controls for the electronic imaging system were simple. The operator selected the ARM CAMERAS command from the menu on the monitor, and the computer set the cameras into the integrate mode of acquiring a single frame. This was done twenty seconds prior to firing time. Two control signals from the range control panel were used to start and stop the camera integration period, similar to opening and closing a film camera shutter. These were the control panel Lockout On and Lockout Off signals, with their actuation timer setting from thumbwheel switches on the panel. To allow for electro-mechanical delays in the gun firing mechanism, the electrical signal firing pulse occurs 1.000 second before T=0. The Lockout On signal was also set at -1.000 second, and the Lockout Off signal at -0.700 second. As soon as the shot was fired, the computer was then accessed, and an image put on the monitor within 30 seconds.

5. LIVE TESTS

During the extent of the installation and testing period, a number of images of live models fired down the range were captured and stored. These were often used by the range personnel for "quick look" information to determine if the shot was good or not. Unfortunately, we did not have enough time to test our algorithms and software for locating the model in 3-space, because all our time was taken in other testing and image processing. Completing these tests is a high priority and should be conducted as soon as sufficient funding is available, to prove the algorithms and accuracy of the location calculations. The images were stored on discs for future reference.

6. 1024v x 512h CCD CAMERA SYSTEM

In conjunction with the studies and algorithm development that Los Alamos has done for Eglin, we invited a vendor to demonstrate a prototype 1024_v x 512_h CCD camera at Eglin during the testing of the proof-of-principle. We had initially made contact with the vendor through Megavision. Because the Megavision Image Processor was already interfaced to the CCD camera, we also invited Megavision to capture some images on the Eglin test range so that we might compare them with the proof-of-principle images and also to verify that the CCD cameras were sensitive enough to work with the Eglin spark gaps.

It took several days to get the Megavision/CCD Camera system operating with the range control signals, but we did manage to capture one test image of a projectile fired in the range. We took many other images of static projectiles for calibration purposes and later transferred those images to the IBM AT system, where we performed some calculations on one image. The Megavision system provided an easily adaptable interface to the CCD camera and also demonstrated image processing capability that would provide the necessary functions for the full-range instrumentation. It would be to Eglin's advantage to do all further algorithm and image processing development on the image processor that will be used on the full range system so that all software developed will be directly usable and not wasted. A small system like the IBM AT does not have sufficient capabilities for the range. The Megavision system is interfaced to the CCD camera, has the necessary capabilities, and would be a good choice.

Even though the CCD camera was a prototype and did not contain a controller or frame buffer, it did show very good performance that appears to meet the range-imaging requirements. Characterization and more testing of the CCD camera should be done next year to support this early work before committing to it for the full range instrumentation.

7. ALGORITHM TESTS

Prior to delivery of the proof-of-principle system to Eglin, the centroid and second-moment-of-inertia algorithms were coded and tested at Los Alamos.

a. Centroid

Because the bead locations are very important in any measurement and because they are also very small in size, we simulated a bead in image memory and used that to test the centroid algorithm. The detailed Eglin bead is shown in Figure 6.

For a 1024_v x 512_h pixel camera, the spatial resolution for a 96_v" x 48_h" field of view (the reflecting screen) is the same for both the horizontal and vertical directions, so we can calculate it using the horizontal dimensions as:

$$R_s = \frac{\text{Field of view dimension}}{\text{Number of pixels}} = \frac{48"}{512 \text{ pixel}} = \frac{0.09375"}{\text{pixel}} \quad (224)$$

Using R_s for both pixel dimensions, a pixel area is then $R_s^2 = 8.789 \times 10^{-3} \frac{\text{square inches}}{\text{square pixel}}$.
We will also assume a viewing situation with the camera that should be the worst case, i.e., most pixels in the camera are only partially covered by the image, as shown in Figure 22. We will, however, arrange the bead such that we can calculate the sub-pixel areas conveniently.
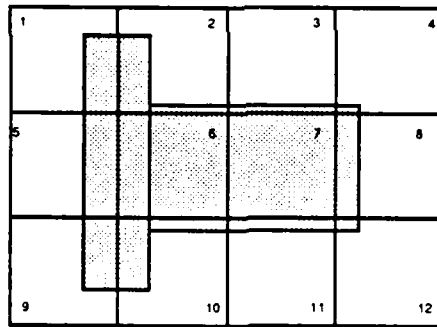

Figure 22. Eglin Bead Image on CCD

The pixels covered by the bead are numbered 1 through 12. The calculated sub-pixel areas of the bead image are listed in Table 3, along with the image processor digitized values rounded to 8-bit integers (the 8-bit digitizer values are 0 for zero area and 254 for an area of 8.789×10^{-3} square inches, or one square pixel).

TABLE 3. BEAD PIXEL AREAS

PIXEL	AREA	VALUE
1	.002180	63
2	.003176	92
3	.001512	44
4	.000443	13
5	.003000	87
6	.008789	254
7	.008789	254
8	.002578	75
9	.002180	63
10	.003175	92
11	.001512	44
12	.000443	13

The digitizer values calculated for the bead were then entered into the image processor memory, resulting in an image shown in Figure 23 (magnified), where pixel values of 254 are white and values of 0 are black.
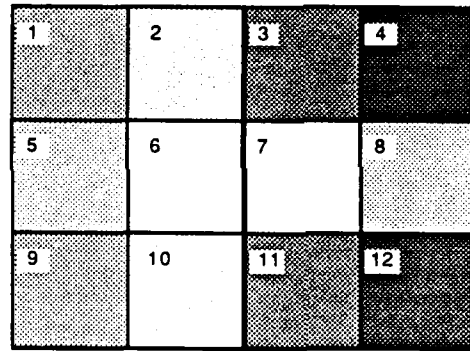

Figure 23. Magnified Bead Image on Monitor

The centroid of the bead has been calculated manually as being along the central horizontal axis and 0.1074" from the left edge (top hat section). This was done by calculating the centroids of the two distinct rectangular areas of the bead, summing the individual moments of the two rectangular areas, and then dividing by the total area, or

$$X_c = \frac{\text{Sum of Area Moments}}{\text{Total Area}} = \frac{0.004056559}{0.037778} = 0.1073789 \qquad (225)$$

Rounding X_c to four places results in

$$X_c = 0.1074 \qquad (226)$$

In the image processor, the center of pixel 1 is location 0,0 for x and y, where y is positive down and x is positive to the right. The location of the left edge of the bead from the center of pixel 5 is then calculated as

$$X_{(\text{left edge})} = \frac{0.09375"}{2} - 0.032" = 0.014875" \qquad (227)$$

51

Then, because the centroid of the bead is 0.1073789" from the left edge, the centroid of the bead relative to the center of pixel 5 (location 0,1) is

$$X_c \text{ (inches)} = 0.014875 + 0.1073789 = 0.1222539" \tag{228}$$

Changing this dimension from inches to pixels (which is what the IBM image processor uses):

$$\text{(theoretical)} \quad X_c \text{ (pixels)} = \frac{0.1222539"}{0.09375"/\text{pixel}} = 1.30404 \text{ pixels} \tag{229}$$

This is the theoretical location of the X dimension at the bead centroid. The Y_c (pixels) is calculated similarly as:

$$\text{(theoretical)} \qquad Y_c \text{ (pixels)} = 1.0 \text{ pixels} \tag{230}$$

The image processor was then allowed to calculate the centroid of the simulated bead image so we could determine the highest accuracy of the algorithm. This is only a theoretical comparison, because the bead image used contains absolutely no noise (the presence of which will reduce the accuracy). In the real world we do have noise, so measurements were also done at Eglin using real images. But it is useful to know the ultimate theoretical precision of the programmed algorithm in the system.

The values calculated by the IBM AT image processor using the programmed centroid algorithm are tabulated in Table 4, with the theoretical values.

TABLE 4. CALCULATED BEAD AREA CENTROIDS

Theoretical X_c	= 1.30426 pixel
Calculated X_c	= 1.3015 pixel
X_c Error	= 0.00276 pixel
Theoretical Y_c	= 1.0 pixel
Calculated Y_c	= 1.0 pixel
Y_c Error	= 0 pixel

It may be seen that the largest error was in the X dimension = 0.00276 pixel. Because the spatial resolution in the image is 0.09375 "/pixel, the error is 0.00276 x 0.09375, or X_C(Error) = 0.000259", which is extremely good relative to the Aeroballistics range requirements. The claimed best case error for the presently used film camera system on the range is 0.03 cm (0.012") for the projectile position (Reference 8). This translates to about 0.024" best case shadowgraph error for the film system by assuming the projectile in the center of the range and using simple geometry. This agrees closely with a calculated film error of about 0.023" determined by the Los Alamos study done in 1985 (Reference 5).

b. Angle

A process similar to the centroid comparison was done to test the second-moment-of-inertia (angle) algorithm in the computer. A small rectangular shape approximately 1.875" long x 0.46875" wide was chosen. The rectangular shape was oriented at an angle corresponding to a rise of Y = 1, X = 5 or

$$\theta \text{(theoretical)} = \text{TAN}^{-1} \frac{1}{5} = 11.30993247° \tag{231}$$

The sub-pixel values could then be calculated precisely because the rectangle image was located advantageously on the imager. The IBM AT image processor second-moment-of-inertia algorithm software calculated an angle as

$$\theta_{(calculated)} = 11.30992° \tag{232}$$

The difference between the theoretical and calculated angles is in error of only 0.00001°. This again is for the case with no noise. But because the angle algorithm also calculates and uses the centroid, we see that the small angle error is very good indeed.

8. MEASUREMENTS AT EGLIN

The only measurements taken at Eglin, limited by the short amount time we had to do other testing, imaging, and installation, were centroids of beads and spatial locations of reference objects. These reference objects were thumbtacks mounted on the screen itself. The tack locations relative to the beads are shown in Figure 24.
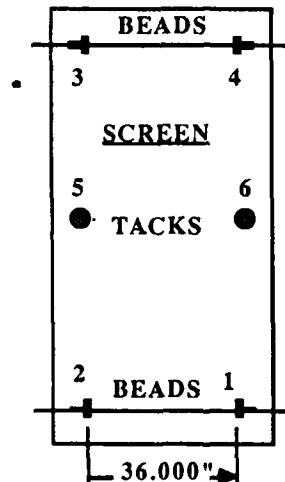

Figure 24. Bead and Tack Locations

The diameters of the two tacks, designated as points 5 (tack 2) and 6 (tack 1) in the image, were measured as:

$$D_5 = 0.3697" \quad and \quad D_6 = 0.3760" \tag{233}$$

Figure 25 is a photograph of the Sony monitor showing an image of the screen taken with the CCD camera. The two bullet shapes are a projectile and its shadowgraph. Tacks 1 (point 6) and 2 (point 5) and beads 1 and 2 are indicated. This image is one of two used for this measurement.

The second image was taken with the GE camera and is similar to the first, but without the projectile. We did not photograph that image.
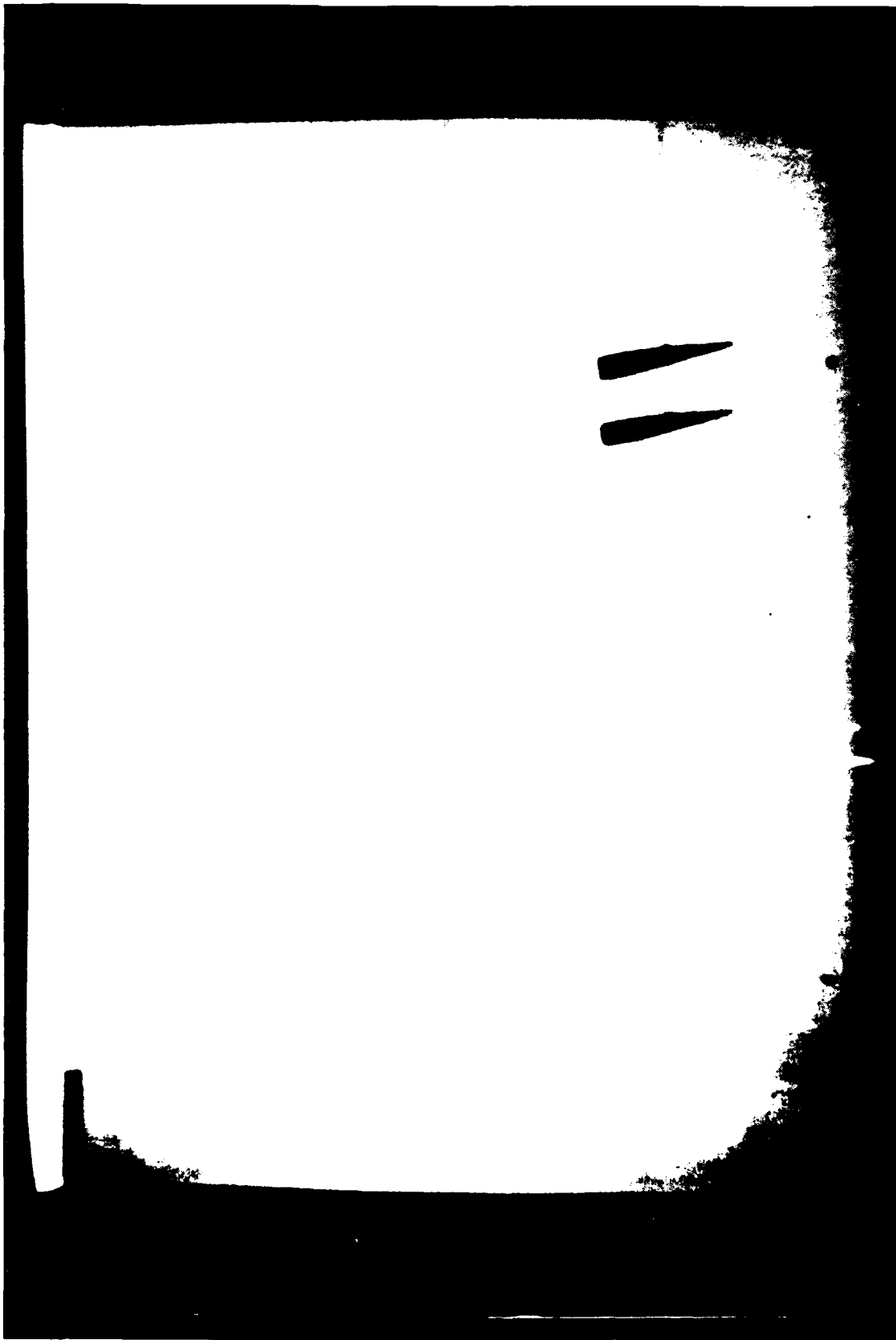
Figure 25. CCD Camera Image

a. Plan

Ideally, we wanted to very accurately measure the distance between the two thumbtacks to use as a standard for comparison with the same measurement obtained by the image processing algorithms run on the IBM AT and by the film cameras. The plan was to:

(1) Measure the distance between the tacks using a tape measure. This is a coarse measurement, but it yields ~ $\frac{1}{16}$ " (0.0625") accuracy.

(2) Photograph the same screen with the existing film camera and measure the distance between the tacks using the normal film reading procedure of the Math Laboratory at Eglin. We are not sure of the accuracy of this measurement, but it should have a probable error of about +/- 0.023", under ideal conditions, because that number was determined by an independent study (Reference 5) by Los Alamos in 1985 by measuring the modulation transfer function (MTF) of the film camera system. Of course, different cameras, lighting, screen conditions, and location of the bead in the image all affect this accuracy. But for now, we will use that measurement of 0.023".

(3) Measure the distance between the tacks with the calibration transit used by the Aeroballistics Research Facility in making range measurements of actual bead locations. This system is probably accurate to about +/- 0.005".

(4) Measure the distance between the tacks with the GE and CCD cameras and using the centroid algorithm.

b. Film Measurement of Tacks

A photograph of the screen was taken and sent to the Math Laboratory at Eglin for reading in the normal fashion, except points 5 and 6 were added, as shown in Figure 25.

Locations of points 5 (tack 2) and 6 (tack 1) are the inside edges, just as the beads are measured. Results of their measurements, in microns, are tabulated in Table 5.

TABLE 5. MATH LABORATORY FILM MEASUREMENTS

POINT #	X (microns)	Y (microns)
1	25395	23197
2	72768	22699
3	703355	110496
4	25938	111096
5	71997	63225
6	25318	63947

Of course, for statistically more reliable data, this measurement should be repeated 10 to 15 times. But, in our case, it was read only once during the time we did this testing.

We know that the inside edges of the beads are set 36.000" apart when they are assembled on the Kevlar line. Any error in that assembly will cause an absolute error in measurements in the range. But the beads are assembled very carefully on pre-stretched line using a machined fixture, so, for now, we will assume no error in this measurement. Measuring the distance between inside edges of the beads on the film, and using 36.000" as the actual distance, allows us to establish the spatial resolution factor for other film measurements.

Because the beads and tacks in the image may be tilted with respect to the camera, we can use simple geometry to find the straight-line distance between them. For the beads, r_b is the straight line distance shown in Figure 26.
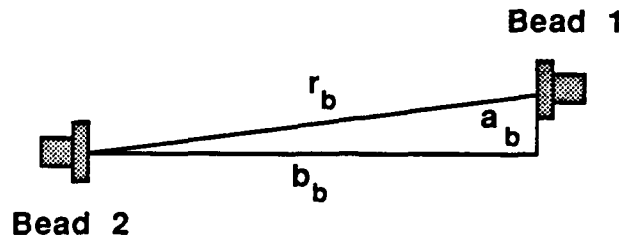
Figure 26. Bead Location Geometry

where
$$a_b = Y_{B2} - Y_{B1} \tag{234}$$

$$b_p = X_{B2} - X_{B1} \tag{235}$$

$$r_b = \sqrt{a_b^2 + b_b^2} \tag{236}$$

So, from the film measurements, we find

$$a_b = 23197 - 22699 = -498 \tag{237}$$

$$b_b = 72768 - 25395 = 47373 \tag{238}$$

$$r_b = \sqrt{(-498)^2 + (47373)^2} = 47375.62 \tag{239}$$

The spatial resolution for the film, then, is:

$$R_{film} = \frac{r_b}{36.000''} = \frac{47375.62}{36.000} = 1315.989444 \ \frac{micron}{inch} \tag{240}$$

Also for the tacks, using the same geometrical calculation for r_T:

$$a_T = 63225 - 63947 = -722 \tag{241}$$

$$b_T = 71997 - 25318 = 46{,}679 \tag{242}$$

and

$$r_T = \sqrt{a_T^2 + b_T^2} \tag{243}$$

$$r_T = \sqrt{(-722)^2 + (46679)^2} = 46684.58 \tag{244}$$

Then applying R_{film} from Equation 240 to the measurement r_T to find the distance between the tacks measured on film, we get

$$D_{T(film)} = \frac{r_T}{R_{film}} = \frac{46684.58}{1315.989375} \tag{245}$$

$$D_{T(film)} = 35.475\text{ "} \tag{246}$$

c. Electronic Imaging Measurement of Tacks

Measuring the tack and bead positions using the centroid algorithm is not as straightforward as it may seem, because of the very important influence of noise in the image. In this case, noise is anything other than the object to be measured. Thus, the Kevlar line, projectile, handprints, and random noise (both optical and electrical) are all "noise." The procedure, then, is to eliminate all extraneous information in the image, taking care not to destroy any measurement information in the object. Any image processing filters or thresholding applied to the image must be such as to comply with the stated procedure. Some of the experimenting at Eglin was an effort to derive some filtering methods to eliminate all the background (set to zero value) and to leave the object (tack or bead) intact. Some procedures were derived by trial and error using knowledge of what affects measurement information, but much image processing development for our measurements needs to be done. This seems to be a relatively new, or at least unpublished, area of image processing; that is, most image processing has to do with improving how an image looks to the human eye, but not in improving measurement capability within an image.

Taking some simple tries at processing an image for eliminating the background, two different images acquired by two different cameras and digitizing systems were operated on to measure the distance between the tacks.

(1) GE Camera Image

The centroid data measured on the GE camera image is shown in Table 6, in pixel units as :

TABLE 6. CENTROID MEASUREMENTS WITH GE CAMERA

Object	X (pixels)	Y (pixels)
Bead 1	459.9247	447.7971
Bead 2	36.4042	446.3474
Tack 1	446.4751	86.324
Tack 2	47.4939	87.3495

Calculating the image spatial resolution using the same geometry as for the film (Figure 26), we get:

$$a_{b(GE)} = 446.3474 - 447.7971 = -1.4497 \tag{247}$$

$$b_{b(GE)} = 36.4042 - 459.9247 = -423.5205 \tag{248}$$

$$r_{b(GE)} = \sqrt{a_b^2 + b_b^2} = \sqrt{(-1.4497)^2 + (-423.5205)^2} \tag{249}$$

$$r_{b(GE)} = 423.52298 \tag{250}$$

However, $r_{b(GE)}$ for the electronic imaging cameras is the distance measured between centroids of the beads (see Figure 6), which should be $36.000" + 2(0.1074") = 36.2148"$. So the spatial resolution on the GE camera image is:

$$R_{(GE)} = \frac{423.52298}{36.2148} = 11.69474859 \ \frac{pixel}{inch} \tag{251}$$

The tack measurements are :

$$a_{T(GE)} = 87.3495 - 86.3240 = 1.0255 \tag{252}$$

$$b_{T(GE)} = 47.4939 - 466.4751 = -418.9812 \tag{253}$$

$$r_{T(GE)} = \sqrt{a_T^2 + b_T^2} \tag{254}$$

$$r_{T(GE)} = 418.9824551 \tag{255}$$

Applying the spatial resolution of the image to the distance between centroids of the tacks, we get

$$D_{TC(GE)} = \frac{418.9824551 \text{ pixel}}{11.69474859 \frac{\text{pixel}}{\text{inch}}} = 35.8265''$$ (256)

Subtracting half of the two tack diameters will give us the distance between the inside edges of tacks, we get

$$D_{T(GE)} = 35.8265 - \frac{0.3697}{2} - \frac{0.3760}{2} = 35.4537''$$ (257)

$$D_{T(GE)} = 35.454''$$ (258)

(2) CCD Camera Image

The centroid data measured on the CCD camera image is shown in Table 7, in pixel units, as :

TABLE 7. CENTROID MEASUREMENTS WITH CCD CAMERA

Object	X (pixels)	Y (pixels)
Bead 1	459.7842	447.1870
Bead 2	36.8718	446.0997
Tack 1	446.8079	86.2711
Tack 2	47.2950	87.7229

Calculating the image spatial resolution using the same geometry as for the film (Figure 26), we find :

$$a_{b(CCD)} = 446.0997 - 447.1870 = -1.0873$$ (259)

$$b_{b(CCD)} = 36.8718 - 459.7842 = -422.9124$$ (260)

$$r_{b(CCD)} = \sqrt{a_b^2 + b_b^2} = \sqrt{(-1.0873)^2 + (422.9124)^2}$$ (261)

$$r_{b(CCD)} = 422.9137976$$ (262)

The spatial resolution on the CCD camera image is

$$R_{(CCD)} = \frac{422.913796}{36.2148} = 11.67792719 \frac{\text{pixel}}{\text{inch}}$$ (263)

59

The tack measurements are:

$$a_{T(CCD)} = 87.7229 - 86.2711 = 1.4518 \tag{264}$$

$$b_{T(CCD)} = 47.2950 - 465.8079 = -418.5129 \tag{265}$$

$$r_{T(CCD)} = \sqrt{a_T^2 + b_T^2} \tag{266}$$

$$r_{T(CCD)} = 418.515412 \text{ pixels} \tag{267}$$

Applying the spatial resolution of the image to the distance between centroids of the tacks, we get :

$$D_{TC(CCD)} = \frac{418.515412 \text{ pixel}}{11.67792717 \frac{\text{pixel}}{\text{inch}}} = 35.8382'' \tag{268}$$

Subtracting half of the two tack diameters will give us the distance between the inside edges of the tacks, we get

$$D_{T(CCD)} = 35.8382 - \frac{0.3697}{2} - \frac{0.3760}{2} = 35.4653 \tag{269}$$

$$D_{T(CCD)} = 35.465'' \tag{270}$$

(3) Tabulation of Measurement Results

Shown in Table 8 are results of the measurement of the spacing between the inside edges of the tacks as:

TABLE 8. MEASUREMENT RESULTS

Method	Tack Measurement
Tape	35.406 "
Film	35.476 "
GE CID	35.454 "
CCD	35.465 "
Transit	35.380 "

60

9. SUMMARY

In summary, the electronic imaging camera measurements resulted in differences of 0.022" and 0.011" from the film system measurement. The error for the film measurement, using the transit measurement as the standard, was 0.096". The errors for the GE and CCD cameras were 0.074" and 0.085", respectively, with the electronic shadowgraph measurements from both cameras closer to the tape and transit measurements than was the film measurement. Not too much should be made of these results, because they are based on so few measurements and they were fairly coarse. Two electronic imaging measurements, with pixel resolutions of about 0.085" agree within 0.011" and they were only 0.011" and 0.022" different from the film measurement, which contains some error. Since the film measurements are so much in error from the transit measurements, something very basic could be wrong with the system or the measuring devices. However, these results for the electronic cameras look very encouraging, and certainly are within the realm of accuracy of the present film camera system, with a distinct possibility of being better.

SECTION VIII

CONCLUSIONS

The work during phase II of the project has accomplished several things that were desired at the beginning, though some results were not anticipated:

a. An Electronic Shadowgraph can achieve equal or better accuracy than the film camera system (using geometric methods), provided that adequate image processing be accomplished and the centroid and second moment of inertia algorithms be used. The centroid and second moment of inertia data can then be used to find the location and orientation of the projectile in 3-space as described in Section VI.

b. Solid state cameras, as opposed to vidicon cameras, are required for their sensitivity to work with the existing Eglin spark-gap as part of an electronic shadowgraph. Vidicon cameras have several deficiencies, the worst of which is inadequate sensitivity for the Eglin application.

c. Solid state cameras with a required resolution to match the film cameras are presently too expensive for the Eglin Range, and are forecast to remain so for at least several years. Cameras with a 2048 x 1024 resolution could cost $50,000 each in 100 quantities, prohibitive for Eglin .

d. Using the centroid and second moment of inertia algorithms along with image processing that does not degrade the measurement information in the image, solid state cameras of 1024 x 512 resolution can be used to replace or augment the film camera system. It is strongly recommended that the electronic shadowgraph system be used to augment the film cameras, and that they both be used in tests for at least a year before reducing dependency on the film cameras. This will allow collection of sufficient data to compare the performance of the two systems and to attain confidence in the electronic camera system.

e. Solid state cameras with 1024 x 512 resolution, adequate sensitivity for the Eglin spark-gap, including an A/D converter and image buffering, and communications logic, has been estimated to cost about $7300 per camera (in 100 quantity) by a leading camera manufacturer and will be available sometime in 1988. This is comfortably within the stated Eglin goal of less than $10,000 per camera.

f. All measurements made during the proof-of-principle installation at Eglin were of a coarse nature and should be verified, but look good in accuracy comparisons with the film system. They do not show what the ultimate accuracy of the electronic camera system could be.

g. Significant development of processes to adequately prepare our images for the application of the measurement algorithms must be done before higher accuracy measurements can be a reality. This could be a major undertaking but may result in some new developments that could be applicable to several Air Force and DoD test and measurement problems.

h. No detailed study of how to locate the spin pin(s) usually placed on projectiles has been done. A cursory calculation has shown that a 2 mm diameter x 4 mm long pin can adequately be located with a 1024 x 512 resolution camera, but this measurement capability must be verified. The possibility exists that locating the centroid and second moment of inertia of the spin pin could also result in more accurate location of the pin, along with proper three-dimensional geometry.

i. Handling of winged or finned objects has not been worked out. This could be a problem that may be solved by proper editing of the image using a priori information about the model. However, much work and experimenting must be done to accomplish it.

SECTION IX

RECOMMENDATIONS

a. It is feasible to begin work aimed at instrumenting the entire Aeroballistics Research Facility with electronic shadowgraph cameras and suitable control and data processing.

b. Continued study of image processing techniques for measurement applications at Eglin should be able to solve those related problems. High accuracy measurements will never be achieved until suitable image processing for extracting objects from images can be done.

c. If development of electronic shadowgraph range instrumentation is to continue, selection of a solid state camera and associated electronics should be a high priority, so that camera testing and characterization can be done prior to delivery of the full complement of cameras, or perhaps even before ordering the final cameras.

d. Selection and purchase of an image processing system/computer should be completed very early to allow all future software development to be directly applicable and useful for Eglin. Use of the Vicom system and the vidicon cameras is discouraged because of its numerous shortcomings for a large scale installation, not the least of which is its clumsiness with camera interfacing. That system is also over four years old and has demonstrated problems that make it unsuitable for good software development and long term use and support.

e. Completing the process of obtaining measurements with the prototype system and obtaining final location and orientation results using Section VI equations should be accomplished soon. The software to implement the equations has been written but not checked out. This is an important step, in that direct comparisons of film camera and electronic camera results can be made for many shots in the range. This will allow compiling confirming data for the electronic cameras and methods, and will be required for proving new image processing techniques on the Eglin images.

REFERENCES

1. R.R. Brown, J.R. Parker, and R.J. Kelley, "System Design Aspects of Using High-Speed Electronic Imaging Techniques in Aeroballistic Research," Proceedings of the ICIASF '85 Record Stanford University, August 1985.

2. D.M. Holt and J.R. Parker, Using the Mini-Optoliner as a Spectral Calibration Source for the Eglin Project, Los Alamos National Laboratory, Los Alamos, New Mexico, December 1986.

3. D.M. Holt, Report on the Eglin Vidicon Camera Resolution Measurement, Los Alamos National Laboratory, Los Alamos, New Mexico, June 1986.

4. A. Higdon and W.B. Stiles, Engineering Mechanics, Second Edition, Prentice-Hall, 1957.

5. R.R. Brown and J.R. Parker, Conceptual Design and Analysis of High-Speed Electronic Imaging, LA-10072-MS, Los Alamos National Laboratory, Los Alamos, New Mexico, November 1984.

6. P.F. Smith, A.S. Gale, and J.H. Neelley, New Analytic Geometry, Revised Edition, Ginn and Co., 1956.

7. Werner Frei Associates, Imagelab™ Model 100, Santa Monica, California 1986.

8. R.L. Kittyle, J.D. Packard, and G.L. Winchenbach, Description and Capabilities of the Aeroballistic Research Facility, AFATL-TR-87-08, Air Force Armament Laboratory, Eglin Air Force Base, Florida, May 1987.

END
DATE
FILMED
7-88
DTIC